Characterization and device physics of polymer semiconducting devices with metal oxide contacts

de Bruyn, Paul

Characterization and device physics of polymer semiconducting devices with metal oxide contacts

Paul de Bruyn

Characterization and device physics of polymer semiconducting devices with metal oxide contacts

Paul de Bruyn
PhD Thesis
University of Groningen

Zernike Institute PhD Series 2018-16
ISSN 1570-1530
ISBN 978-94-034-0706-7 (print)
ISBN 978-94-034-0705-0 (digital)

The work described in this thesis was performed in the research group Molecular Electronics of the Zernike Institute of Advanced Materials and was financially supported by the Zernike Institute for Advanced Materials and the Dutch Polymer Institute under DPI project 660.

DPI
The Polymer Research Platform

university of groningen / faculty of science and engineering / zernike institute for advanced materials

university of groningen

Characterization and device physics of polymer semiconducting devices with metal oxide contacts

PhD thesis

to obtain the degree of PhD at the
University of Groningen
on the authority of the
Rector Magnificus Prof. E. Sterken
and in accordance with
the decision by the College of Deans.

This thesis will be defended in public on

Tuesday 15 May 2018 at 11.00 hours

by

Paul de Bruyn

born on 2 July 1986
in Leek

Supervisor
Prof. P.W.M. Blom

Assessment Committee
Prof. J.C. Hummelen
Prof. B. Noheda Pinuaga
Prof. R.A.J. Janssen

Table of contents

Chapter 1

Introduction

This chapter starts by giving a short overview of the important historical milestone discoveries in the fields of organic- and metal oxide semiconductors. It also outlines the importance of metal oxide semiconductors in organic electronics. The basic physics of the electronic devices that are used in the rest of this thesis are then described and it closes with a description of the general experimental methods used in this thesis.

1.1 Motivation and outline of this thesis

Organic semiconductors and more particularly polymeric semiconductors are characterized by alternating single and double chemical bonds in their carbon backbones, also called a conjugated system. This chemical structure gives rise to a particular energetic structure with delocalized electrons along the backbone of the polymer. σ-bonds, formed from the s-and p- orbitals of the constituent atoms, primarily covalently bond the carbon atoms together, while π-bonds are formed from the overlapping π-orbitals in the chain. The discovery of electrical conduction in these systems dates back to 1977, for doped polyacetylene. [1] In the past decades the development of organic semiconductors has strongly progressed. The promise of low-cost, flexible electronics has stimulated the imagination of the scientific community. As a result, the number of publications in this field of research has increased exponentially. The interdisciplinary nature of this subject has caused a strong collaboration between the physics and chemistry disciplines to design new materials with desired properties and attempt to relate these properties to performance in opto-electronic devices. The developments in utilizing organic semiconductors in electronic devices have progressed especially rapidly in instances, where their properties lend themselves well for the intended application, *e.g.* when high extinction coefficients or electroluminescence is required. For this reason the areas of organic light-emitting diodes (OLEDs) and organic photovoltaics (OPVs) have developed especially quickly, with OLEDs already displaying performance comparable to their inorganic counterparts. [2] Presently, one of the major drawbacks of organic semiconductor technologies is stability. Most organic materials and the materials commonly used as electrical contacts are prone to oxidation and serious questions have arisen on the morphological stability of *e.g.* donor-acceptor blends in OPV. One of the proposed solutions is combining organic with inorganic materials that possess better ambient and morphological stability. Semiconducting transition metal oxides are one of the most prominent candidates to fill this role. In particular zinc oxide (ZnO) and titanium dioxide (TiO_2) have proven to be valuable electron acceptor and contact materials in a wide variety of device structures. [3] Other commonly used materials include molybdenum trioxide (MoO_3), vanadium pentoxide (V_2O_5) and tungsten trioxide (WO_3). [4] Chapter 2 describes the realization of inverted polymer:fullerene solar cells with a ZnO electron transport layer. The

ZnO layer is produced by a low-temperature method based on using a zinc acetylacetonate hydrate solution. In Chapter 3 an extensive characterization of these precursor based ZnO layers produced by this method is presented. In Chapter 4 application of this solution processed low-temperature ZnO in polymer light-emitting diodes is described. An alternative for the precursor based ZnO are layers based on ZnO nanoparticles. In Chapter 5 the use of nanoparticle based ZnO as middle electrode in solution-processed organic tandem solar cells is presented. Contact energetics and the diffusion current in organic devices with a non-Ohmic contact are investigated in Chapter 6. The band structure of ZnO/organic devices is elucidated with this formalism. Finally, Chapter 7 investigates charge injection into organic materials from a non-Ohmic contact, further building on the formalism developed in Chapter 6.

1.2 Metal oxide devices

Semiconducting metal oxides are historically influential semiconducting materials. Early investigations go back as far as 1874, with Schuster's fortuitous discovery of current rectification in aged copper wires, by virtue of the cuprous oxide formed on the surface. [5] This was followed up by the discovery of the cuprous oxide (Cu_2O) rectifier by Grondahl and Geiger [6] and described by Schottky in 1929. [7] More recently, the field of semiconducting metal oxides has seen a resurgence. Undoubtedly the success of the dye-sensitized solar cell (DSSC) since the work of O'Regan and Grätzel in 1991 [8] has spurred the use of most notably TiO_2 and ZnO in current organic electronics research. ZnO is the topic of a plethora of research as a transparent conducting oxide. [9] Application as a replacement of indium tin oxide (ITO) as transparent conducting electrode is most prominent in this regard. [10]Apart from the research on the oxides themselves, significant efforts are ongoing to combine them with organic materials in *e.g.* OLEDs and OPVs. Two primary applications of metal oxides in organic electronics are either as electron acceptor or electron injection/extraction layer. Hybrid devices with ZnO as electron acceptor processed both from nanoparticle dispersions and from a precursor material which is hydrolyzed in-situ, have been demonstrated. [11,12] Additionally, the use as injection layer in OLEDs in what is now dubbed HyLED (hybrid light emitting diode) and their use as extraction layer in inverted structure OPVs have been received with great interest. [13] In more complex device structures, such as multi-junction OPVs, ZnO and TiO_2 have found use in the interconnecting layer, where charges originating from the sub-cells have to recombine. [14] The advantage of metal oxide contacts lies predominantly in stability, as they usually replace highly oxygen and moisture sensitive low work-function metals such as barium or calcium as electron injecting contact. [15] There are, however, some requirements for the metal oxides to fulfill to be fully compatible with the low-cost processing of organic materials. First of all, they should be processable from solution. The aim for organic electronics is to ultimately process large-area devices on a fully solution based coating procedure. Thus if one wants to make use of metal oxide materials, the processing should be made compatible with such a large scale coating procedure. Secondly, they should require only a low-temperature annealing procedure. Most organic semiconductor materials degrade at too

high temperatures and additionally the flexible substrates that are aimed to be used for printing are not compatible with high temperatures either.

1.3 Device principles

The device principles of OLEDs and OPVs are essentially the same, yet all processes occur in reverse order. In OLED devices, charges first have to be injected from the electrodes into the organic material, after which excitons have to be formed from charges of opposite sign. These should subsequently recombine to the ground state to emit photons. In OPVs, photons have to be absorbed by the organic material, form excitons, after which these excitons have to be split into free charge carriers and collected at the electrodes. Apart from such a general description, there are of course subtle differences. The least subtle of all is the presence of two separate organic materials in OPVs, contrary to just one material in OLEDs. The large exciton binding energy in organic materials necessitates the need to deliver a driving force for charge separation. This resulted in what is now known as the bulk heterojunction concept. In general terms, a donor and an acceptor material are intimately mixed to create a phase separated layer with internal interfaces. The energetic offset between both the donor and acceptor lowest unoccupied molecular orbital (LUMO) and highest unoccupied molecular orbital (HOMO) levels provides the driving force for separating the exciton into free charges in their respective donor and acceptor phases. Furthermore the requirements on the electrodes are different for OLEDs and OPVs. Because the acceptor material in OPVs has a deeper LUMO level than the donor materials typically used, the work function of the contact electrode can be higher to maintain ohmic contact to this acceptor level. This facilitates usage of contact materials that are more resistant to atmospheric oxidation and in general broadens the range of materials that can be selected. Since the donor materials that are generally used for OPVs are of a similar composition as the materials used for OLEDs, more reactive materials have to be used for the electrodes in these devices, thus creating a need for better encapsulation to protect the devices against atmospheric oxygen and moisture.

1.4 Device fabrication & characterization

All devices presented in this thesis were processed as described below, unless otherwise noted. The devices were fabricated on patterned ITO substrates. These substrates were cleaned with a non-ionogenic detergent and demi-water, before being ultrasonically agitated in acetone and 2-propanol consecutively. Substrates were then spun dry and dried in an oven at 140 °C before being subjected to UV-ozone cleaning for 20 minutes. All organic materials were spin cast in an inert N_2 environment. Poly(3,4-ethylenedioxythiophene):poly(styrenesulfonate) (PEDOT:PSS) was spin cast in air to yield thicknesses of ~50 nm. In all instances Clevios P VPAI 4083 was used. ZnO layers were processed by spin casting a 20 mg/mL solution of zinc acetylacetonate hydrate ($Zn(acac)_2$) in ethanol at 50 °C in air onto substrates held at 50 °C as well and subsequently annealing the substrate to 120 °C for 5 minutes to hydrolyse the precursor complex, resulting in ZnO layers of ~15 nm. V_2O_5 was processed from a vanadium oxytriisopropoxide solution, diluted in isopropanol to varying degrees, typically 1 to 50 parts. Vacuum evaporation of all materials (metals, MoO_3, LiF) was done under high vacuum ($<10^{-6}$ mBar) through appropriate shadow masks to create patterned devices. In general, in organic devices the active organic layer is sandwiched between charge transport layers (or metals directly) on an ITO substrate with a metal top contact. I-V measurements of all devices are carried out by an automated program using a Keithley 2400 Sourcemeter. Quantum efficiency measurements were carried out by using a broad spectrum Tungsten halogen lamp, a set of narrow band-pass filters with a full width half maximum (FWHM) of 10 nm and a calibrated silicon reference photodiode.

1.5 References

1. Chiang, C. K., Fincher Jr, C. R., Park, Y. W., Heeger, A. J., Shirakawa, H., Louis, E. J., and MacDiarmid, A. G., *Physical review letters*, 39, 17 (1977), 1098.

2. Sasabe, H. and Kido, J. , *Journal of Materials Chemistry C*, 1, 9 (2013), 1699-1707.

3. Oh, H., Krantz, J., Litzov, I., Stubhan, T., Pinna, L., and & Brabec, C. J. , *Solar Energy Materials and Solar Cells*, 95, 8 (2011), 2194-2199.

4. Tokito, S., Noda, K., and Taga, Y. , *Journal of Physics D: Applied Physics*, 29, 11 (1996), 2750.

5. Schuster, A. , *The London, Edinburgh, and Dublin Philosophical Magazine and Journal of Science*, 48, 318 (1874), 251-258.

6. Grondahl, L. O. and Geiger, P. H. , *Journal of the AIEE*, 46, 3 (1927), 215-222.

7. Schottky, W. and Deutschmann, W. , *Physikalische Zeitschrift*, 30 (1929), 839.

8. O'regan, B. and Grätzel, M. , *nature*, 353, 6346 (1991), 737-740.

9. Özgür, Ü., Alivov, Y. I., Liu, C., Teke, A., Reshchikov, M., Doğan, S., and Morkoc, H. , *Journal of Applied Physics*, 98, 4 (2005), 11.

10. Liu, Y. and Lian, J., *Applied Surface Science*, 253, 7 (2007), 3727-3730.

11. Huang, J., Yin, Z., and Zheng, Q. , *Energy & Environmental Science*, 4, 10 (2011), 3861-3877.

12. Moet, D. J., Koster, L. J. A., de Boer, B., and Blom, P. W. M. , *Chemistry of materials*, 9, 24 (2007), 5856-5861.

13. Bolink, H. J., Coronado, E., Repetto, D., and Sessolo, M. , *Applied Physics Letters*, 91, 22 (2007), 223501.

14. Kim, J. Y., Lee, K., Coates, N. E., Moses, D., Nguyen, T. Q., Dante, M., and Heeger, A. J. , *Science*, 317, 5835 (2007), 222-225.

15. Hau, S. K., Yip, H. L., Baek, N. S., Zou, J., O'Malley, K., and Jen, A. K. Y. , *Applied Physics Letters*, 92, 25 (2008), 225.

Chapter 2

A facile route to inverted polymer solar cells using a precursor based zinc oxide electron transport layer

In this chapter inverted polymer:fullerene solar cells with ZnO and MoO_3 transport layers are demonstrated. ZnO films are prepared through spin casting of a zinc acetylacetonate hydrate solution, followed by low temperature annealing under ambient conditions. The performance of solar cells with an inverted structure is shown to be equivalent to that of conventional cells with a bottom-anode-top-cathode configuration for three efficient polymer:fullerene systems.

2.1 Introduction

One of the drawbacks of solar cells based on polymers is the use of poly(3,4-ethylene dioxythiophene) (PEDOT) doped with poly(4-styrenesulfonate) (PSS), since the ITO/PEDOT:PSS interface is not stable and has an adverse affect on organic device performance over time.[1,2] Inverted devices utilizing an evaporated metal oxide/metal anode (e.g. MoO_3/Al) instead of PEDOT:PSS have shown comparable performance to their conventional counterparts.[3-6] Furthermore, zinc oxide (ZnO) has successfully been applied as a low work function cathode in organic tandem solar cell devices,[7] and even as acceptor material in polymer:ZnO bulk heterojunctions.[8-10] In the nanoparticle approach, ZnO nanoparticles (nc-ZnO) of approximately 5 nm in diameter were synthesized by hydrolysis and condensation of zinc acetate dihydrate by KOH in methanol, using the method of Pacholski et al.[11] Furthermore, MoO_3 has been used in organic light emitting diodes as the anode material in several studies.[12-16] To further simplify the processing and exclude the nanoparticle synthesis, we introduce a simple, low temperature solution process to fabricate ZnO films for electronic devices. This alternative process for the ZnO cathode involves spin casting and subsequent pyrolysis of the precursor material zinc acetylacetonate ($Zn(acac)_2$) hydrate. This material has been shown to react with H_2O to form ZnO at low temperatures and high humidity conditions in metal-organic chemical vapor deposition (MOCVD) experiments.[17] The proposed mechanism for such a low temperature decomposition is that the high humidity conditions prevent dehydration of the hydrated material and enable a single step conversion of the precursor to ZnO at temperatures below 120 °C, making the process compatible with a large amount of organic materials and devices. In this Chapter, we demonstrate inverted solar cells with precursor ZnO electron transport layers for three well-studied polymer:fullerene systems, *i.e.* based on poly(3-hexylthiophene) (P3HT), poly[9,9-didecanefluorene-*alt*-(bis-thienylene) benzothiadiazole] (PF10TBT) and poly[2,6-(4,4-bis-(2-ethylhexyl)-4H-cyclopenta[2,1-*b*;3,4-*b'*]dithiophene)-*alt*-4,7-(2,1,3-benzothiadiazole)] (PCPDTBT). As an acceptor the standard [6,6]-phenyl-C_{61}-butyric acid methyl ester (PCBM) has been used. All three blends can provide power conversion efficiencies in excess of 4% in combination with a fullerene acceptor.[18-20] Our inverted solar cell structures using precursor ZnO exhibit a performance that is identical to conventional bottom-anode-top-cathode geometry solar cells.

2.2 Results and discussion

To investigate the optical absorbance and work function of the precursor ZnO films, UV-vis spectroscopy and Kelvin probe measurements were performed. First 20 mg/mL of $Zn(acac)_2$ hydrate (obtained from Sigma-Aldrich) was dissolved in ethanol, stirred for several hours at 50 °C and subsequently filtered with a 0.2 μm pore size PTFE filter. ITO covered glass substrates were cleaned with soap and deionised water, followed by ultrasonic treatment in acetone and 2-isopropanol. Afterwards they were dried in an oven at 140 °C for ten minutes in ambient conditions, followed by UV-ozone treatment for twenty minutes. $Zn(acac)_2$ was spin cast after both solution and substrates were heated to 50 °C. Hydrolysis of the precursor was carried out in air during thirty seconds on a hotplate at 120 °C. ZnO typically requires UV illumination to transform from an intrinsic semiconductor into an n-type material by desorption of O_2^- radicals from the surface.[21,22] After illumination with a Steuernagel SolarConstant 1200 metal halide lamp, a reduction of the work function from 4.2 eV to 3.7 eV was measured with a Kelvin probe calibrated to a gold reference. This is in line with the assumption of injection of electrons into the conduction band by UV illumination and a corresponding raise of the Fermi level. The optical absorbance of a 20 nm layer of ZnO was measured with respect to a glass reference with a Perkin-Elmer Lambda 900 spectrophotometer and is shown in Figure 1. Note the excellent optical transparency in the visible range of wavelengths of the precursor made ZnO film. The optical absorbance of the precursor layer before conversion is shown for reference.

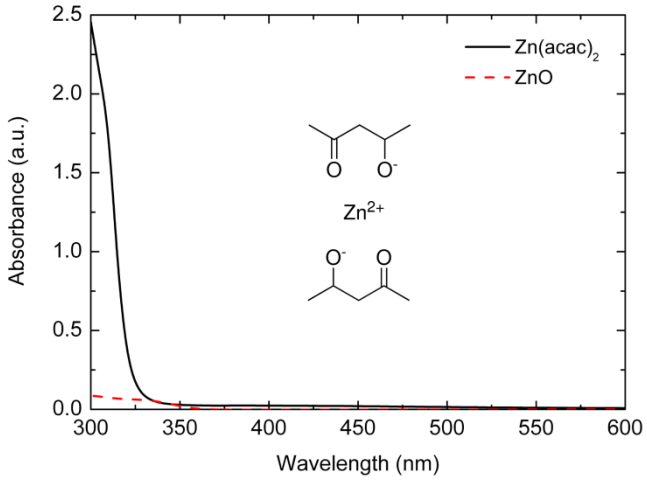

Figure 1. Optical absorbance of a 20 nm layer of ZnO. The absorbance of the $Zn(acac)_2$ precursor layer is shown for reference. The inset shows the chemical structure of $Zn(acac)_2$.

P3HT:PCBM (1:0.8 by weight, 15 mg/mL of polymer) was dissolved in chloroform. PCPDTBT:PCBM (1:2.5 by weight, 7 mg/mL of polymer) was dissolved in a chlorobenzene solution containing 1.5 wt% 1,8-octanedithiol, which was added to increase the photovoltaic performance of the resulting devices as described in literature.[18,23] PF10TBT:PCBM (1:4 by weight, 3 mg/mL of polymer) was dissolved in pristine chlorobenzene. ITO substrates were cleaned as described before. PEDOT:PSS (Clevios P VP Al 4083) was spin cast in air to yield a 50 nm layer on the substrate. Spin casting of the P3HT:PCBM and PCPDTBT:PCBM blends was done in a nitrogen atmosphere, while PF10TBT:PCBM was spin cast in air. Thermal evaporation was performed at a pressure of 10^{-6} mbar for all materials (LiF, Al and MoO_3). Finished cells were illuminated through illumination masks with a Steuernagel SolarConstant 1200 metal halide lamp, calibrated to 1 sun intensity and corrected for spectral mismatch with the AM1.5G spectrum using a Si reference cell. The calculated mismatch factors for P3HT:PCBM, PF10TBT:PCBM and PCPDTBT:PCBM in this setup amounted to 1.40, 1.40 and 1.03, respectively.[24] Electrical characterization was done with a Keithley 2400 SourceMeter.

Figure 2 shows the structure of the completed cells, along with the materials used for the active layers. The current density-voltage characteristics of the

P3HT:PCBM:PCBM, PF10TBT:PCBM and the PCPDTBT:PCBM cells under illumination are shown in Figure 3. All photoactive layers were approximately 80 nm thick. Table 1 shows the performance parameters for all solar cells presented in this study.

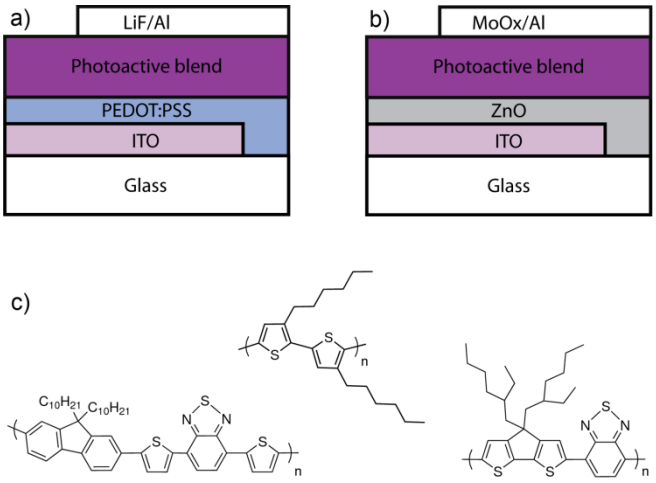

Figure 2. Solar cell geometries and polymers used in this study. a) Conventional bottom-anode-top-cathode structure. b) Inverted bottom-cathode-top-anode structure. c) Chemical structures of PF10TBT (left), P3HT (middle) and PCPDTBT (right).

Photoactive layer	Type	J_{sc} [A m^{-2}]	V_{oc} [V]	FF [%]	MPP [mW cm^{-2}]
PF10TBT:PCBM	Conventional	67.3	0.96	61	4.0
	Inverted	66.1	0.95	59	3.7
P3HT:PCBM	Conventional	87.6	0.57	0.66	3.2
	Inverted	91.5	0.59	0.60	3.2
PCPDTBT:PCBM	Conventional	91.8	0.61	50	2.8
	Inverted	91.4	0.58	50	2.6

Table 1. Photovoltaic properties of conventional and inverted PF10TBT:PCBM and PCPDTBT:PCBM solar cells under 1 sun white light illumination.

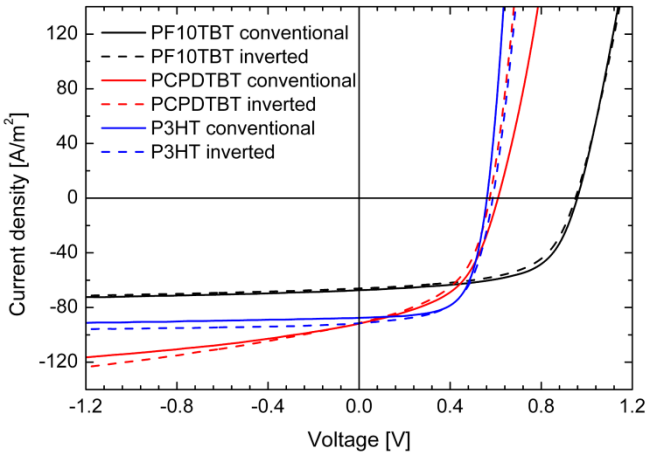

Figure 3. *J-V* characteristics of solar cells employing both contact geometries for the two material blends. 'Inverted' denotes the bottom-cathode-top-anode structure.

We observe that the performance parameters and thus the cell efficiencies are very close for cells with the conventional and inverted geometry. The reported efficiencies are in good agreement with previously published values for optimized PF10TBT:PCBM cells.[19] The efficiency of the PCPDTBT:PCBM cells has been increased in comparison to a previous publication, which is due to decreased recombination by addition of 1,8-octanedithiol in these devices.[23,25] Furthermore, optical absorption simulations based on the transfer matrix formalism have been performed on the two structures for the PF10TBT:PCBM blend.[26-29] The optical constants needed for this simulation were obtained with variable angle spectroscopic ellipsometry.[19,30] As can be seen in Figure 4, the calculated integrated exciton generation rates for both the conventional and inverted are equal to within 1% for the two structures.

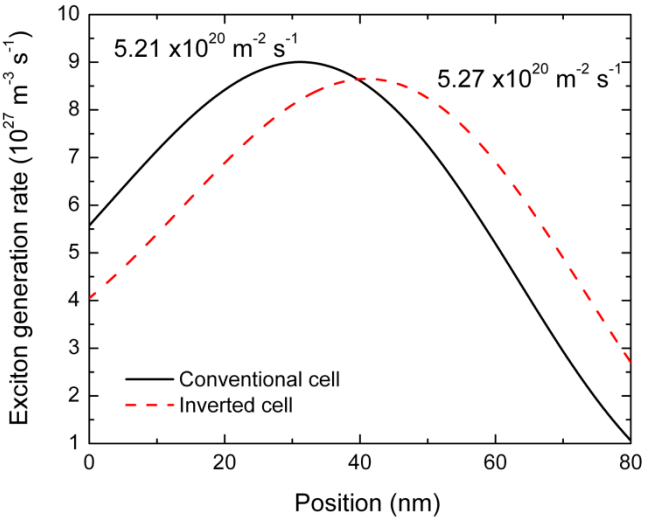

Figure 4. Simulated exciton generation rates in conventional and inverted geometry cells. The origin is defined as the substrate side of the device. The integrated generation rates are shown for the two geometries.

This validates the experimentally observed equal short-circuit currents under the assumption of equal internal quantum efficiencies. In this treatment the origin is defined as the point in the photoactive layer where the light first enters the device, *i.e.* the substrate side. For the conventional device the light is directly reflected at the aluminium top electrode, whereas for the inverted device the 10 nm of MoO_x acts as an optical spacer, thereby changing the shape of the absorption envelope.

2.3 Conclusions

In summary, we have shown the electrical operation of inverted solar cells with an ITO/ZnO cathode, fabricated through the low temperature decomposition of $Zn(acac)_2$. The performance of these cells is shown to be equivalent to cells made in the conventional bottom anode, top cathode geometry. In the next chapter the spin-cast films of ZnO obtained from thermal decomposition of zinc acetylacetonate hydrate will be further characterized.

2.4 References

1. M. P. de Jong, L. J. van IJzendoorn, and M. J. A. de Voigt, *Appl. Phys. Lett.* 77, (2000), 2255-2257.

2. K. W. Wong, H. L. Yip, Y. Luo, K. Y. Wong, W. M. Lau, K. H. Low, H. F. Chow, Z. Q. Gao, W. L. Yeung, and C. C. Chang, *Appl. Phys. Lett.* 80, (2002), 2788-2790.

3. C. Tao, S. Ruan, X. Zhang, G. Xie, L. Shen, X. Kong, W. Dong, C. Liu, and W. Chen, *Appl. Phys. Lett.* 93, (2008), 193307-3.

4. G. Li, C. Chu, V. Shrotriya, J. Huang, and Y. Yang, *Appl. Phys. Lett.* 88, (2006), 253503-3.

5. H. Liao, L. Chen, Z. Xu, G. Li, and Y. Yang, *Appl. Phys. Lett.* 92, (2008), 173303-3.

6. F. C. Krebs, *Organic Electronics* 10, (2009), 761-768.

7. J. Gilot, M. M. Wienk, and R. A. J. Janssen, *Appl. Phys. Lett.* 90, (2007), 143512-3.

8. D. J. D. Moet, L. J. A. Koster, B. de Boer, and P. W. M. Blom, *Chemistry of Materials* 19, (2007), 5856-5861.

9. W. Beek, M. Wienk, and R. Janssen, *Advanced Materials* 16, (2004), 1009-1013.

10. S. D. Oosterhout, M. M. Wienk, S. S. van Bavel, R. Thiedmann, L. Jan Anton Koster, J. Gilot, J. Loos, V. Schmidt, and R. A. J. Janssen, *Nat. Mater.* 8, (2009), 818-824.

11. C. Pacholski, A. Kornowski, and H. Weller, *Angewandte Chemie International Edition* 41, (2002), 1188-1191.

12. T. Matsushima, Y. Kinoshita, and H. Murata, *Appl. Phys. Lett.* 91, (2007), 253504-3.

13. X. Jiang, Z. Zhang, J. Cao, and W. Zhu, *Solid-State Electronics* 52, (2008), 952-956.

14. H. You, Y. Dai, Z. Zhang, and D. Ma, *J. Appl. Phys.* 101, (2007), 026105-3.

15. H. Lee, S. W. Cho, K. Han, P. E. Jeon, C. Whang, K. Jeong, K. Cho, and Y. Yi, *Appl. Phys. Lett.* 93, (2008), 043308-3.

16. D. Y. Kim, J. Subbiah, G. Sarasqueta, F. So, H. Ding, Irfan, and Y. Gao, *Appl. Phys. Lett.* 95, (2009), 093304-3.

17. T. Arii and A. Kishi, *Journal of Thermal Analysis and Calorimetry* 83, (2006), 253-260.

18. M. Morana, M. Wegscheider, A. Bonanni, N. Kopidakis, S. Shaheen, M. Scharber, Z. Zhu, D. Waller, R. Gaudiana, and C. Brabec, *Advanced Functional Materials* 18, (2008), 1757-1766.

19. L. H. Slooff, S. C. Veenstra, J. M. Kroon, D. J. D. Moet, J. Sweelssen, and M. M. Koetse, *Appl. Phys. Lett.* 90, (2007), 143506-3.

20. M. Lenes, G. A. H. Wetzelaer, F. B. Kooistra, S. C. Veenstra, J. C. Hummelen, and P. W. M. Blom, *Advanced Materials* 20, (2008), 2116-2119.

21. F. Verbakel, S. C. J. Meskers, and R. A. J. Janssen, *Appl. Phys. Lett.* 89, (2006), 102103-3.

22. W. J. E. Beek, M. M. Wienk, M. Kemerink, X. Yang, and R. A. J. Janssen, *J. Phys. Chem. B* 109, (2005), 9505-9516.

23. J. Peet, J. Y. Kim, N. E. Coates, W. L. Ma, D. Moses, A. J. Heeger, and G. C. Bazan, *Nat. Mater.* 6, (2007), 497-500.

24. J. M. Kroon, M. M. Wienk, W. J. H. Verhees, and J. C. Hummelen, *Thin Solid Films* 403-404, (2002), 223-228.

25. M. Lenes, M. Morana, C. J. Brabec, and P. W. M. Blom, *Advanced Functional Materials* 19, (2009), 1106-1111.

26. J. D. Kotlarski, P. W. M. Blom, L. J. A. Koster, M. Lenes, and L. H. Slooff, *J. Appl. Phys.* 103, (2008), 084502-5.

27. L. A. A. Pettersson, L. S. Roman, and O. Inganas, *J. Appl. Phys.* 86, (1999), 487-496.

28. H. Hoppe, N. Arnold, D. Meissner, and N. S. Sariciftci, *Thin Solid Films* 451-452, (2004), 589-592.

29. N. Persson, H. Arwin, and O. Inganas, *J. Appl. Phys.* 97, (2005), 034503-8.

30. D. Moet, M. Lenes, J. Kotlarski, S. Veenstra, J. Sweelssen, M. Koetse, B. de Boer, and P. Blom, *Organic Electronics* 10, (2009), 1275-1281.

Chapter 3

Characterization of precursor-based ZnO transport layers in inverted polymer solar cells

In this chapter a wide range of characterization techniques are presented to study spin-cast films of ZnO obtained from thermal decomposition of zinc acetylacetonate hydrate. Additionally inverted cells possessing this layer were prepared. Deposition conditions of the solution onto the substrate (e.g. substrate temperature) were found to be crucial in order to obtain well-performing inverted cells. Interestingly, it is demonstrated that full conversion of the precursor into crystalline ZnO is not necessary to prepare well-performing cells.

3.1 Introduction

Over the last years, increasing efforts were devoted to the research and development of organic electronics produced on flexible substrates. In particular, an interesting new generation of photovoltaic (PV) cells involves the use of semiconducting polymers. The latter are very promising materials as they are soluble in many organic solvents, allowing deposition by solution printing or coating. Among the materials used as electron transport layer, *n*-type metal oxides have received considerable attention due to their enhanced ambient stability over organic materials and high optical transparency. In particular zinc oxide (ZnO) is a promising material due to its environmental stability, high transparency and compatibility with various deposition techniques. Two main strategies to prepare ZnO buffer layers from solutions were explored over the past years:

(i) synthesis of ZnO nanoparticles followed by a dispersion in a given solvent to obtain a colloidal suspension of nanoparticles, which can be processed by different methods such as spin coating or slot die coating at room temperature without any (thermal) post-deposition treatment, [1,2]

(ii) dissolution of a precursor in a solvent which is deposited on a substrate by spin coating or printing [3,4]; the conversion from the precursor to ZnO occurs after deposition on the substrate.

In the first case, the nanoparticle characteristics and properties are mainly determined by the synthesis parameters and are not expected to be dramatically modified by the deposition step, which can typically be performed at room temperature. Nevertheless, per definition, colloidal suspensions made of nanoparticles dispersed in a solvent system are metastable. As a result, they may undergo aggregation upon storage due to, for example, temperature changes. Additionally, modifying the dispersing medium can significantly alter the aggregation state of the nanoparticles. [1]

When the precursor approach is utilized, the properties of the final ZnO layer are strongly dependent on sample history and method of preparation. In other words, adjusting processing and post-deposition parameters (e.g. temperature)

is crucial in order to tune ZnO layer properties and hence the final performance of the OPV device.

In view of future industrial manufacturing of OPV cells in which all layers are solution-processed, it is crucial to process transparent conductive oxide (TCO) layers from solution in order to avoid more costly vacuum steps. Moreover, in order to use these layers in R2R produced devices manufactured on plastic substrates such as polyethylene terephthalate (PET) or polyethylene naphthalate (PEN), low-temperature deposition of metal oxide layers is highly desirable. The insertion of such R2R compatible, solution-processed ZnO layers in inverted and tandem solar cells as part of low work function cathodes [1,5,6] and recombination layers [7,8], respectively, has already been reported in literature. Such a layer has also been used to prepare solution-processed cells free from Indium Tin Oxide (ITO), see e.g. reference [9].

Solar cells with a precursor-based zinc oxide transport layer and low reflective light absorber were demonstrated in Chapter 2. Here, zinc acetylacetonate hydrate ($Zn(acac)_2$. H_2O) dissolved in ethanol was spin-cast on ITO and annealed at 120 ºC for 30 s. The performance of solar cells with an inverted structure, namely ITO/ZnO/ photoactive layer (PAL)/MoO_3/Al, was shown to be equivalent to the ones of conventional cells with a bottom anode- top cathode configuration for various conjugated polymers.

To elucidate which requirements this electron transport layer (ETL) must fulfill as part of well performing organic solar cells, a systematic study is warranted. In this chapter, we present a study of zinc acetylacetonate-based zinc oxide layers. A broad range of techniques such as focused-ion beam scanning electron microscopy (FIB-SEM), X-Ray diffraction (XRD) and X-Ray reflectivity (XRR), thermogravimetric analysis (TGA), Modulated Differential Scanning Calorimetry (MDSC), Fourier-transform infrared (FTIR) spectroscopy and Atomic Force Microscopy (AFM) are used to characterize the exact nature of the layer before and after precursor conversion. Additionally, solar cells were prepared by varying in a systematic way the ZnO layer deposition to determine a suitable processing window for this layer.

3.2 Experimental section

Sample preparation: Zinc acetylacetonate hydrate ($C_{10}H_{14}O_4Zn \cdot H_2O$ or $Zn(acac)_2 \cdot H_2O$) was purchased from Sigma-Aldrich (99.995 % purity) and used as received. Solutions of 20 mg/mL in ethanol were prepared by dissolving the precursor at 50 ºC under stirring for several hours. The solution was subsequently filtered with a 0.45 µm PTFE filter. Clean glass substrates sonicated in acetone and isopropanol were used as substrates. $Zn(acac)_2$ – ethanol solutions were spin-cast on the glass substrates which had undergone an UV-ozone treatment in order to improve the wetting on the substrate during spin coating.

Solar cells were prepared by cleaning ITO coated glass substrates with a non-ionogenic detergent, before sonication in acetone and 2-propanol. Substrates were dried in an oven and cleaned by UV-ozone before spin casting procedures. PEDOT:PSS (Clevios VPAI 4083) was spin cast under ambient conditions. $Zn(acac)_2$ solutions from ethanol were spin cast at 50 °C and subsequently annealed at 120 °C. P3HT:PCBM blends (1:0.8 by weight) were spin cast in a nitrogen-filled glovebox. The solar cells were finished off with either a 1 nm LiF/100 nm Al cathode or a 10 nm MoO_3/100 nm Au anode, thermally evaporated under vacuum ($p < 10^{-6}$ mbar).

3.3 Measurements

In-situ IR measurements were performed using a Thermo Nexus FTIR bench equipped with a heatable Golden Gate ATR Module. Samples made of thin films of $Zn(acac)_2$-ethanol solution spin-cast on gold-coated silicon substrates were directly brought into contact with the Golden Gate ATR Module initially set at 40 °C. Directly after a given sample was brought into contact with the module, the temperature of the latter was set either at 120 °C or at 200 °C (maximum reachable temperature). FTIR spectra were subsequently recorded every 10 s during 30 minutes.

FIB-SEM: Sample preparation: The $Zn(acac)_2$-ethanol solution was spin-cast on glass substrates and subsequently annealed for 20 s at 120 ºC. Afterwards, the samples were coated in a sputter coater with a few-nm thick Pt layer to avoid charging. Milling was subsequently done with a Ga+ ion gun to open a trench in the sample. The electron gun for SEM is at a 42 º angle to the FIB column. As a result, it was possible to study cross-sections of the studied layers by tilting the sample. The study was done with a Philips Nova 200 Nanolab SDB (Small Dual Beam).

XRD and XRR measurements: $Zn(acac)_2$ – ethanol solution was spin-cast on a glass plate in the same conditions as those used to prepare solar cells. The spin-cast layers were subsequently annealed at 120 °C or 250 °C for various times. The samples were subsequently characterized with a PANalytical X'Pert PRO MPD diffractometer equipped with a Cu X-ray source and X'Celerator detector. Due to the low thickness of the samples studied, Grazing Incidence (GI) measurements were performed. XRR measurements were performed to determine the ZnO layer thickness.

J-V measurements of the solar cells performed done with a computer controlled Keithley 2400 SourceMeter. Quantum efficiency was measured with a setup built in-house.

3.4 Results and discussion

Since the ETL layer studied here comes from the thermal decomposition of a precursor, leading to the formation of a metal oxide, it is apparent that the *post*-deposition parameters (e.g. annealing temperature, residual humidity of the atmosphere) strongly influence the composition of the layer. Less obvious is the influence of the deposition parameters themselves. It appears that the temperature of deposition of the $Zn(acac)_2$ – ethanol solution is crucial as the base morphology is strongly influenced by the processing.

Layers prepared by spin coating of $Zn(acac)_2$-ethanol on glass substrates maintained either at room temperature or heated at 50 °C were characterized by optical microscopy, see **Figure 1**. When the sample was spin-cast with a solution maintained at room temperature or heated at 50ºC on a non-heated glass substrate, "needle-like" crystallized features were visible, see **Figure 1a**. It is worth noting that these features were observed before thermal annealing of the $Zn(acac)_2$ layer and remained unchanged after thermal treatment. In other words, the presence of these features is not related to the precursor decomposition and ZnO formation, but is rather linked to the $Zn(acac)_2$ properties. On the contrary, when the deposition was done on a pre-heated substrate (**Figure 1b**), the optical microscope analysis did not reveal the presence of any needle features. Most probably, in the second case, the elevated temperature of the substrate during deposition promotes rapid solvent evaporation before supersaturation of the $Zn(acac)_2$-ethanol solution and therefore hinders $Zn(acac)_2$ crystallization.

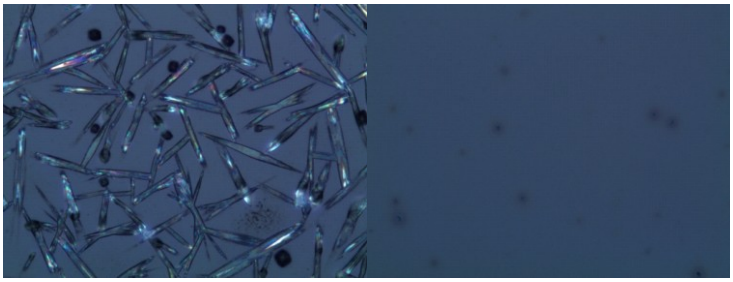

Figure 1. Optical microscope pictures of $Zn(acac)_2$ layers spin-cast from an ethanol solution on: (a) a non-heated substrate and (b) a substrate heated at 50 °C. Picture size: 31.1 × 98.3 μm².

FIB-SEM analysis gives more insight regarding the structure of these two types of layers. **Figure 2** displays pictures of the cross-sections of a layer prepared on a non-heated substrate (corresponding to **Figure 1a**). These layers were very rough and irregular; some of the needle features were as high as 140 nm (see **Figure 1c**). Locally the substrate was not even covered, resulting in the presence of holes in the layer.

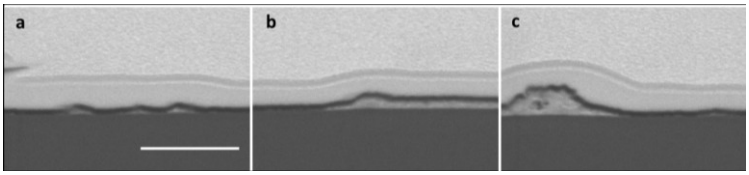

Figure 2 a-c. FIB-SEM pictures of the cross-section of a $Zn(acac)_2$ layer spin-cast on a non-heated substrate and subsequently annealed at 120 °C for 20 s. Scale bar: 400 nm.

On the contrary, layers resulting from the spin coating of $Zn(acac)_2$-ethanol solution on heated substrates appeared to be closed and smooth with homogeneous thickness over the whole coated area, see **Figure 3** (several locations checked).

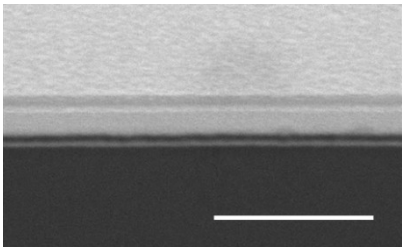

Figure 3. FIB-SEM picture of a cross-section of a $Zn(acac)_2$ layer spin-cast on a pre-heated substrate and subsequently annealed at 120 °C for 20 s. Scale bar: 400 nm.

To evaluate the exact roughness of the second type of layers, i.e. the closed layer displayed in **Figure 3**, AFM measurements were performed on the surface of the layers. **Figures 4a** and **4b** show a top-down view of a flat layer

sample surface and a visualization of the layer in 3D, respectively. The RMS roughness of the layer, as determined from these images amounts to 1.7 nm.

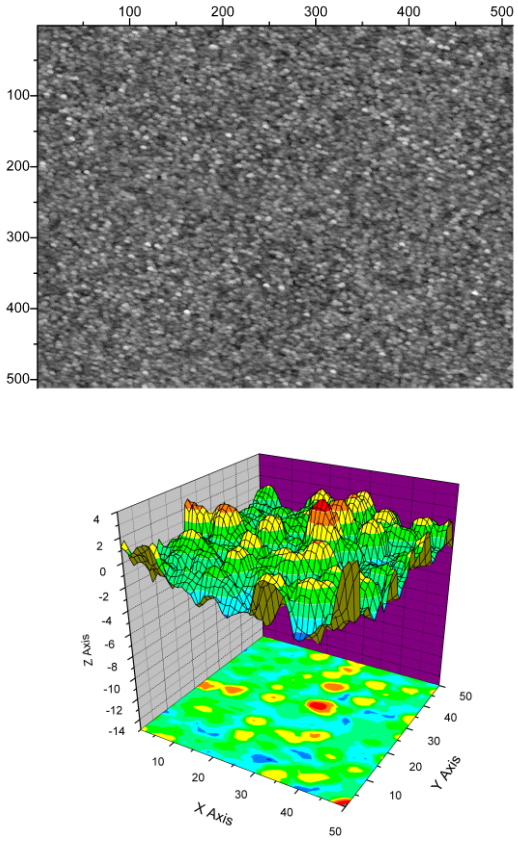

Figure 4. a. AFM picture of a 'closed' ZnO layer b. reconstruction of the layer in 3D.

Inverted cells prepared with smooth and rough $Zn(acac)_2$ layers were prepared. The results of the EQE and J-V measurements are shown in **Figures 5a and 5b**, respectively. It is immediately obvious from the comparison of the J-V characteristics that the fill factor of the solar cell with the 'open' ZnO layer is much lower than the solar cell with the 'closed' ZnO layer. This can be attributed to direct contact between the ITO substrate and the organic materials. The higher work function of ITO as compared to ZnO causes a misaligned electron extraction contact in the regions of direct contact, resulting

in a lowered fill factor. This simultaneously explains the magnitude of the measured dark current, as shown in the inset of **Figure 5b**. Hole current can directly flow between the MoO_3 contact and the exposed ITO contact, resulting in an increase in the diode dark current. Furthermore the short-circuit current density is largely unaltered, exhibited as well by the quantum efficiency measurements depicted in **Figure 5a**. The subtle spectral differences could be explained by a difference in light scattering between the two ZnO layer structures.

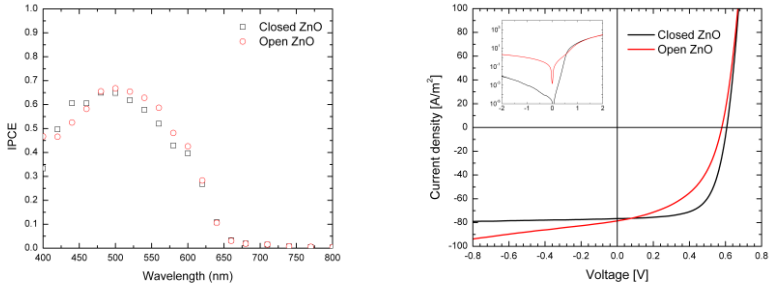

Figures 5. a. *EQE and* ***b.*** *J-V measurement results for inverted cells prepared with smooth (i.e. 'close') and rough (i.e. 'open') ZnO layers.*

Upon heating, zinc acetylacetonate decomposes to form zinc oxide. This decomposition reaction has been studied in depth by Arii et al. [10] Here, we aim to gain more insight regarding the decomposition of $Zn(acac)_2$ for use in electron transport layers for inverted solar cells. [5]

The decomposition of zinc acetylacetonate monohydrate ($Zn(acac)_2 \cdot H_2O$) was monitored by TGA under controlled atmosphere. The typical TGA curves for the precursor decomposition in dry nitrogen and in air (heating rate of 10 °C/min) is shown in **Figure 6**. MSDS-TGA measurements performed on the same sample (not shown) evidenced that the precursor undergoes four endothermic transitions at comparable temperatures as the ones reported.[10] Mass losses occur in two main steps: one around 80-100 °C, and a second one from about 100 °C to 180 °C. At the end of the heating step, a small amount of residue remains in the crucible.

According Arii and Kishi,[10] the precursor undergoes the following decomposition reaction:

$Zn(CH_3COCHCOCH_3)_2.\ H_2O \rightarrow$

$2\ CH_3COCH_2COCH_3 + ZnO$ (1)

The first endothermic transition occurs between 80 and 100 °C. It is accompanied by a mass loss of 6.5 %, which is due to dehydration as it corresponds to the theoretical, calculated mass loss expected from the thermal dehydration of one molecule of water. After this first transition, upon heating, the mass loss occurred in three successive steps which could clearly be evidenced with the differential gravimetric (DTG) thermograph (not shown). The three other endothermic transitions observed at temperatures higher than 100 °C were identified as the sum of sequential and parallel reactions including phase transition, fusion, evaporation and decomposition of $Zn(acac)_2$.[10] An important finding of the work of Arii and Kishi is that ZnO formation from $Zn(acac)_2$ occurs via the formation of an intermediate compound in dry nitrogen. The exact nature of this compound was not clearly identified.

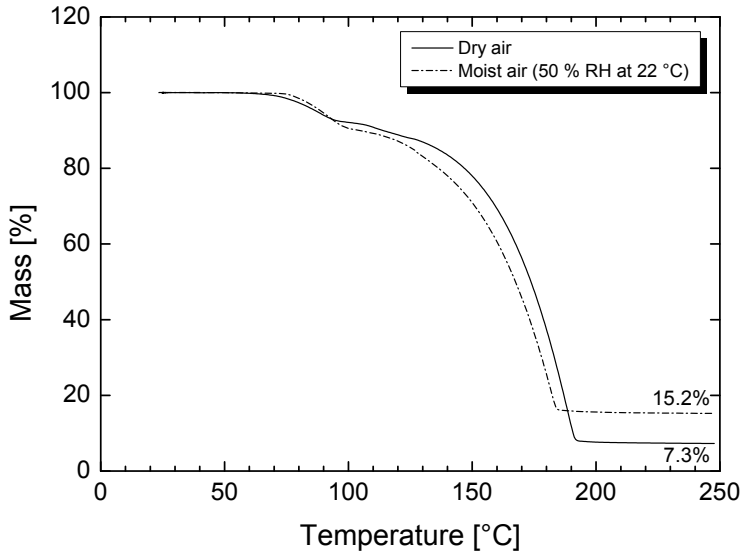

Figure 6. TGA results of $Zn(acac)_2$ in dry and moist air (relative humidity of 50 %) for a heating rate of 10 °C/min.

After heating in dry nitrogen, the weight percentage of the remaining residue made of ZnO equals 7.3 % at 200 ºC, which is only 24 % of what could theoretically have been formed. This result gives a clue that sublimation of the precursor occurs during the heating of the sample. When the precursor decomposition was carried out in wet nitrogen with 50 % relative humidity (i.e. the level of humidity maintained in our clean room), the ZnO formation, thus the reaction yield, was increased significantly from 7.3 % to 15.2 % of the sample initial weight. These results were in line with the findings of Arii et al. and correspond to the lowest absolute humidity level examined.[10] The latter found that water vapor introduced in the atmosphere could prevent $Zn(acac)_2$ sublimation during heating and therefore enhanced ZnO formation.

The above-mentioned inverted cells using a $Zn(acac)_2$-based ETL were annealed at only 120 °C, [5] suggesting that the precursor decomposition process was not complete. Nevertheless, it was found by Arii and Kishi that moisture present in the atmosphere plays the role of catalyst during the reaction of decomposition of the precursor, promoting the formation of ZnO even at relatively low temperatures. To confirm this, XRD measurements were performed on $Zn(acac)_2$ layers prepared in the same conditions as the ETL used in the inverted cells. The precursor solution was spin-cast on two heated glass substrates. The resulting layer was subsequently annealed at 120 °C for 30 s and 4 hours. The results of these measurements are presented in **Figure 7**. The broad peak present at 20 º comes from the glass substrate. It can be seen that, even after 30 s annealing at 120 ºC, crystallization peaks corresponding to crystalline ZnO can be evidenced. The peaks are rather broad, most probably due to a small crystallite size. The difference of intensity of the signal at 35 º might indicate a difference in crystallite orientation. Protracted annealing time at 120 °C did not significantly increase the degree of crystallinity of the layer.

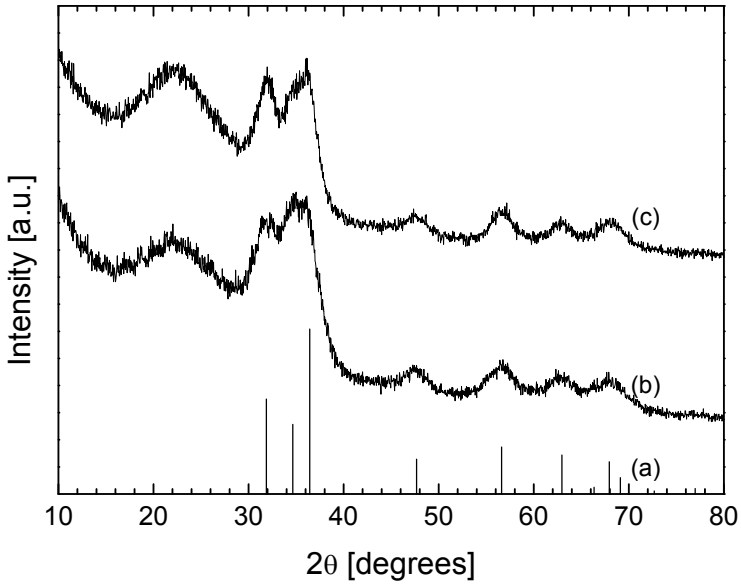

Figure 7. Standard XRD pattern of ZnO **(a)** and grazing incidence diffractograms of the spin-cast ZnO layers after annealing at 120 °C for 20 s **(b)** or 2 h **(c).**

X-ray reflectivity measurements indicated the presence of a layer possessing a density much lower than the one of bulk ZnO(< 3 g/cm^3)[11] and a thickness of about 26 nm, which is of the same order of magnitude as the layer thickness measured by FIB-SEM, see **Figure 3**.

Interestingly, samples annealed for 30 s or 2 hours at a temperature at which full $Zn(acac)_2$ conversion is expected, i.e. 250 °C, based on TGA analysis (**Figure 6**), did not display a significantly higher degree of crystallinity than the samples annealed at 120 °C (not shown).

To get more insight in the chemical composition of the ETLs, FTIR measurements were performed on layers spin-cast on gold-coated silicon substrates. The first spectrum taken before annealing of the layer was characteristic of $Zn(acac)_2$,see **Figure 8a**. After the sample was heated at 200 °C for 20 s, nearly complete conversion of $Zn(acac)_2$ could be observed since the two bands in the 1300-1800 cm^{-1} wavelength range were no longer visible (**Figure 8c)**. On the contrary, spectra recorded after 30 s of heating at 120 °C showed a significant, though incomplete, conversion of the precursor, see **Figure 8b**. This evidences that the $Zn(acac)_2$ thermal decomposition takes

place within seconds in the experimental conditions used to prepare inverted OPV cells. Additionally, it could be evidenced that the $Zn(acac)_2$ thermal decomposition was not complete while carried out at 120 °C, even after protracted heating (e.g. up to 2 hours – not shown). Although XRD measurements evidenced that part of the precursor was effectively converted into crystalline ZnO, these FTIR measurements suggest that the ETL obtained after $Zn(acac)_2$ decomposition at low temperature, i.e. 120 °C, most probably consists of a mixture of small ZnO crystals coexisting with another compound. The most likely candidate for this residual compound is hydrozincite, or $Zn_5(CO_3)_2(OH)_6$, based on the spectral match with the experimental results and the fact that it is a common secondary mineral of ZnO. [12]

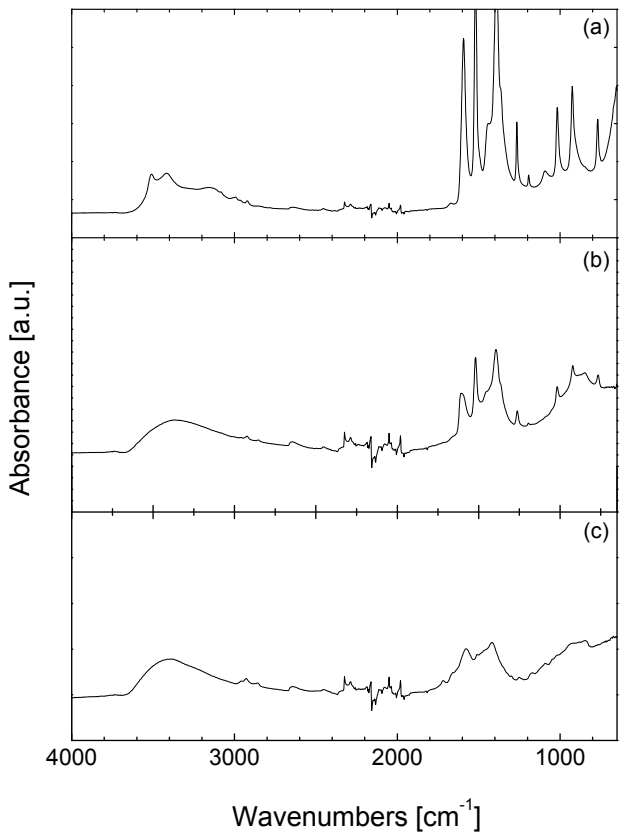

Figure 8. IR spectra of samples with spin-cast $Zn(acac)_2$ layers on glass after various heat treatments: **(a)** as spin-cast, **(b)** annealed at 120 °C for 30 s and **(c)** annealed at 200 °C for 20 s.

3.5 Conclusions

Preparation of ZnO ETC layers from thermal decomposition of $Zn(acac)_2$ precursor has been shown to be a promising way to prepare inverted OPV cells exhibiting performance comparable to the corresponding conventional cells with a bottom-anode-top-cathode configuration. It is evidenced that the conditions in which the $Zn(acac)_2$ solution is deposited, namely the substrate temperature, are determining to get a close, smooth layer. The latter is indeed a requirement to prepare well-performing cells.

Furthermore, the results of this study indicate that protracted heating times and/or high annealing temperatures are not required to trigger the formation of ZnO from the $Zn(acac)_2$ precursor in order to produce well-performing cells. Though it does not lead to complete conversion of $Zn(acac)_2$ to ZnO, a short 20-s annealing at 120 °C is sufficient. In this respect, this indicates that pure ZnO ETC layers are not required since partly crystalline ZnO-based ETC layers can perform as well as crystalline ZnO ETC layers obtained after full conversion of the precursor (i.e. annealing at 200°C).

3.6 References

1. F. C. Krebs, Y. Thomann, R. Thomann, J. W. Andreasen, *Nanotechnology*, 19, (2008), 424013.

2. F. C. Krebs, *Sol. En. Mater. Sol. Cells*, 93, (2009), 465.

3. S. T. Meyers, J. T. Anderson, C. M. Hung, J. Thompson, J. F. Wager, D. A. Keszler, *J. Am. Chem. Soc.*, 130, (2008), 17603.

4. R. C. Hoffmann, S. Dilfer, A. Issanin, J. J. Schneider, *Phys. Status Solidi A*, 207, (2010), 1590.

5. P. de Bruyn, D. J. D. Moet, P. W. M. Blom, *Org. Electron.*, 11, (2010), 1419.

6. N. Grossiord, J. M. Kroon, R. Andriessen, P. W. M. Blom, *Org. Electron.*, 13, (2012), 432.

7. J. Gilot, I. Barbu, M. M. Wienk, R. A. J. Janssen, *Appl. Phys. Lett.*, 90, (2007), 1435.

8. D. J. D. Moet, P. De Bruyn, J. D. Kotlarski, P. W. M. Blom, *Org. Electr.*, 11, (2010), 1821.

9. F. C. Krebs, *Org. Electron.*, 10, (2009), 761.

10. T. Arii, A. Kishi, *J. Therm. Anal. Cal.*, 83, (2006), 253.

11. U. Seetawan, S. Jugsujinda, T. Seetawan, C. Euvananont, C. Junin, C. Thanachayanont, P. Chainaronk, V. Amornkitbamrung, *Solid State Sc.*, 13, (2011), 1599.

12. W. Preis, H. Gamsjäger, *J. Chem. Thermodynamics*, 33, (2001), 803.

Chapter 4

All-solution processed polymer light-emitting diodes with air stable metal-oxide electrodes

In chapters 2 and 3 the use of precursor based ZnO in organic solar cells was discussed. In this chapter an all-solution processed polymer light-emitting diode (PLED) is presented, using spin-cast precursor zinc oxide (ZnO) and vanadium pentoxide (V_2O_5) as electron and hole injecting contact, respectively. We compare the performance of these devices to the standard PLED design using PEDOT:PSS as anode and Ba/Al as cathode. We show that the all-solution processed PLEDs have an equal performance as compared to the standard design directly after fabrication. However, the ambient stability of the PLEDs with spin-cast transition metal oxide electrodes is exceptionally good in comparison to the standard design.

4.1 Introduction

Polymer light emitting diodes hold the promise of large-area lighting at low cost.[1] However to achieve low costs all material layers in the device, including the injecting contacts, should be deposited from solution to fully benefit from a cheap production method such as roll-to-roll processing. In practice this excludes the use of low work function metal contacts, since they generally have to be evaporated in vacuum and are extremely sensitive to oxygen and moisture. The use of these metals is necessary to ensure efficient electron injection into the lowest unoccupied molecular orbital (LUMO) of the light emitting polymer due to its low electron affinity of typically 2-3 eV. This low electron affinity of light-emitting polymers intrinsically provides a great challenge for the air stability of the electron injecting contact.[2] Transition metal oxides such as zinc oxide (ZnO) and titanium oxide (TiO_x) have proven to be promising candidates for overcoming this problem. Specifically, systems with *evaporated* molybdenum trioxide (MoO_3) as hole injecting contact and ZnO or TiO_x as electron injecting contact have been studied extensively.[3,4] The enhanced hole injection properties of MoO_3 compared to poly(3,4-ethylenedioxythiophene):poly(4-styrenesulfonate) (PEDOT:PSS), especially when injecting into polymers with very deep HOMO levels, has been abundantly proven in literature.[5–10] Furthermore, thermally evaporated vanadium pentoxide (V_2O_5) has been shown to provide an ohmic injecting contact to luminescent polymers and polymer:fullerene solar cells as well.[11–14] However, a big challenge to overcome is the realization of metal oxide electrodes that are processed from solution, combining efficient charge injection with air stability. A solution-based process to produce amorphous V_2O_5 has already been developed in the last century[15–17] and has recently been revisited and introduced as anode in organic solar cells by Larsen-Olsen et al.[18] Here we introduce organic light emitting diodes with ZnO and V_2O_5 injecting contacts through a fully solution deposited and low temperature route. ZnO and V_2O_5 can be fabricated as described in chapters 1 and 2. For the emitting polymer, we chose the polyfluorene copolymer PF10TBT. An advantage of this red-emitting polymer compared to for example a poly(p-phenylene vinylene) (PPV) based polymer is its higher electron affinity. Its LUMO is located typically 3.4 eV below vacuum (as compared to 2.9 eV for PPV), making it easier to inject electrons from the ZnO cathode, which has a work function of typically ~4 eV. Furthermore, PF10TBT exhibits a good ambient

stability allowing us to demonstrate the stability of the contacts and to distinguish between contact and polymer degradation upon exposure to air. In Fig. 1 the device layouts of the various devices presented in this study are shown.

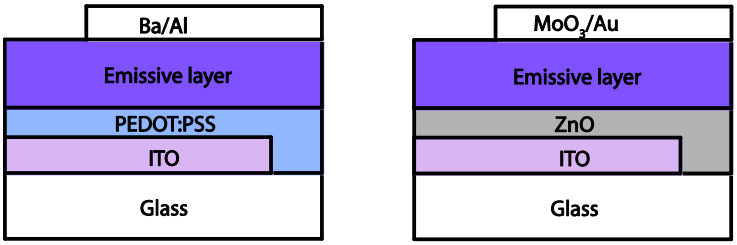

Figure 1. Device structures of the devices presented in this study. Conventional structure (left) and inverted structure (right).

4.2 Results and discussion

In order to evaluate the performance of the spin-cast ZnO cathode and V_2O_5 anode separately we first make use of a test device (Fig. 1). This inverted device contains a spin-cast ZnO cathode as bottom contact and an evaporated MoO_3/Au hole injecting contact as top contact. This evaporated MoO_3/Au anode has been proven to be an Ohmic contact on polyfluorene derivatives with a very deep HOMO level (-6.0 eV below vacuum).[5] As a result also on the PF10TBT polymer studied here, with the HOMO level at -5.4 eV, we can be sure that this hole contact is ohmic, enabling to investigate the performance of the spin-cast ZnO cathode. As a first step the electrical characteristics of the inverted devices with a solution processed ZnO electron injecting bottom contact and an evaporated MoO_3/Au hole injecting top contact are compared to conventional devices with a PEDOT:PSS and Ba/Al contact for hole and electron injection, respectively. Fig. 2 shows the current density-voltage (*J-V*) and light-output-voltage (*L-V*) characteristics (Fig. 2a), as well as the ratio of the light output and the current as a function of voltage (Fig. 2b), which is a measure for the PLED efficiency. The inset of Fig. 2b shows the current of the devices on a double log scale.

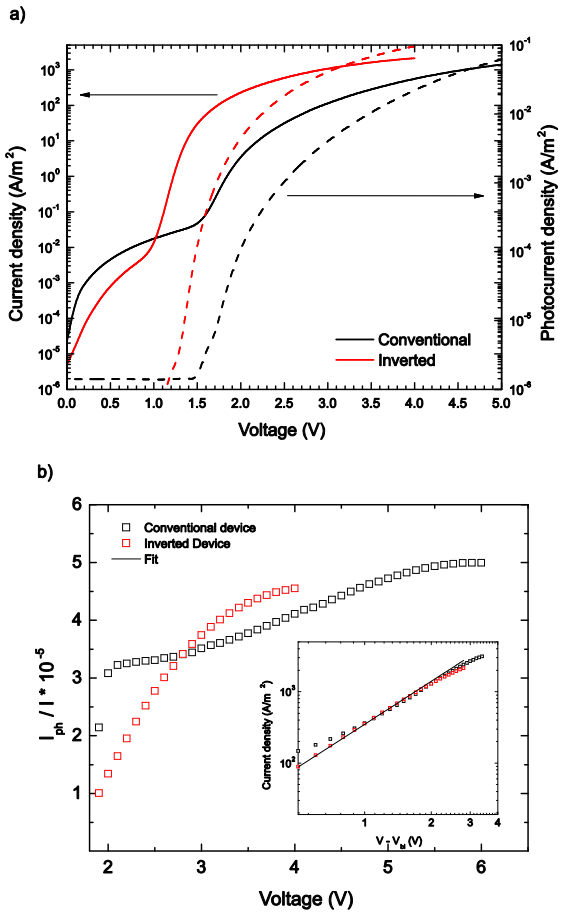

Figure 2. Performance comparison of the conventional and inverted LEDs. a) comparison of *J-V* (solid lines) and *L-V* (dashed lines) characteristics and b) relative PLED efficiency. The inset of b) shows the current on a log-log scale, as well as a fit to the space charge limited current model of eq. 1.

First of all, what can be discerned is close congruence between the efficiencies of the two architectures. The charge injection properties of the ZnO contact will be further discussed in chapter 5. For a PLED with ohmic contacts the current density in the plasma limit is given by[19]

$$J = \left(\frac{9\pi}{8}\right)^{1/2} \varepsilon_0 \varepsilon \left(\frac{2q\mu_p \mu_n (\mu_p + \mu_n)}{\varepsilon_0 \varepsilon B}\right) \frac{(V - V_{bi})^2}{L^3} = \frac{9}{8} \varepsilon_0 \varepsilon \mu_{eff} \frac{(V - V_{bi})^2}{L^3}, \qquad (1)$$

with J the current density, ε_0 the permittivity of vacuum, ε the relative dielectric constant of the polymer, μ_p and μ_n the hole and electron mobility, B the bimolecular recombination constant, V the applied voltage and L the thickness of the polymer layer. Taking $\varepsilon = 3$ and $L = 80$ nm, the effective mobility μ_{eff} derived in this fashion from Fig. 2b amounts to 6.0×10^{-9} m^2/Vs, in agreement with previous determinations.[20] Furthermore, a decrease in the turn-on voltage is observed, as previous publications have shown as well.[3] Next we consider the ambient stability of these devices under two conditions, a) storage in air and b) operation in air. Fig. 3a and 3b show the pristine and the J-V characteristics after 24 hours of storage in air of the conventional and inverted devices, respectively. The normal geometry device has lost most of its functionality after 24 hours of storage in air, while the inverted geometry device remains intact.

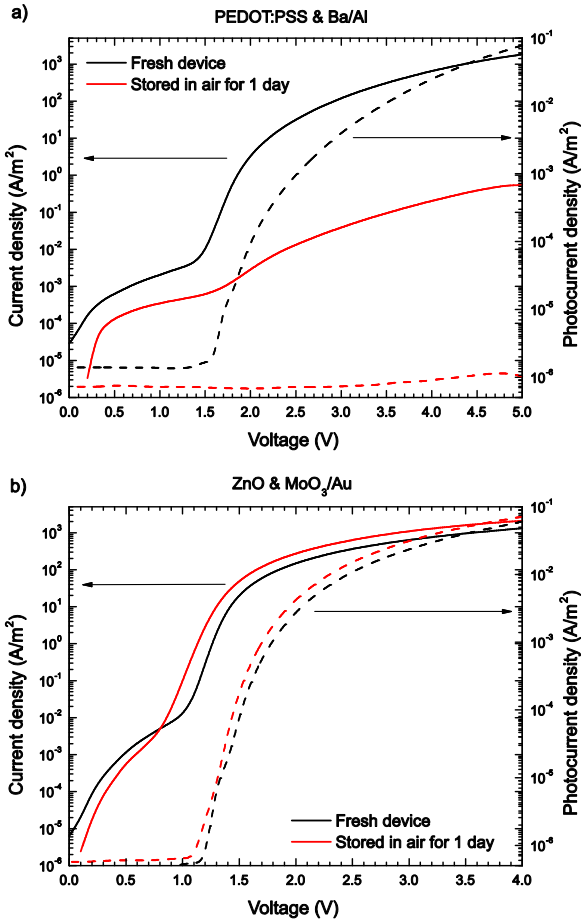

Figure 3. Storage stability of a) conventional and b) inverted geometry devices. Shown are the *J-V* and *L-V* curves in both cases.

Besides the storage stability, also the operational stability is essential. Fig. 4a and 4b show the *J-V* curves for pristine devices and after operation in air for 24 hours at 10^3 A/m^2 for conventional and inverted geometry LEDs, respectively.

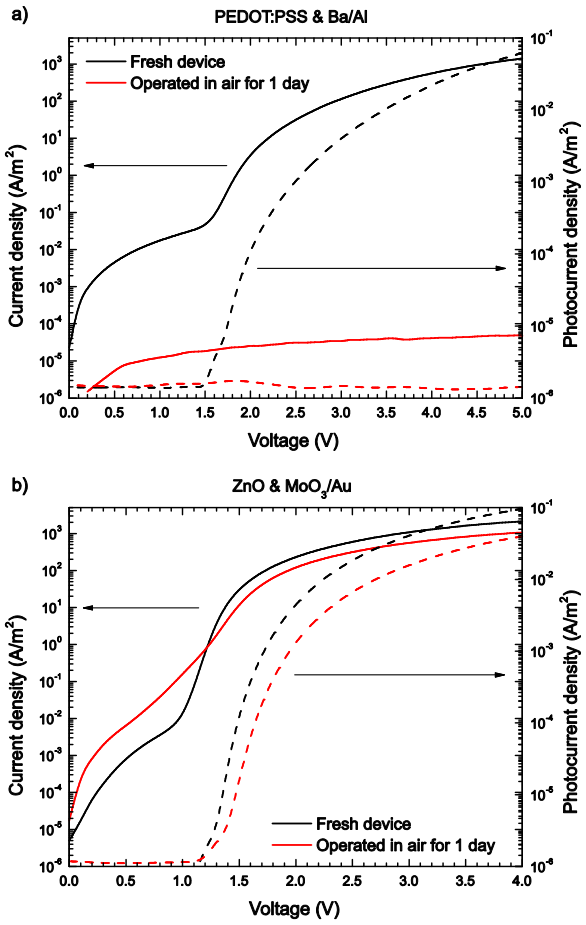

Figure 4. Operational stability of a) conventional and b) inverted geometry devices. Shown are the *J-V* and *L-V* curves in both cases.

The conventional device degrades rapidly in air as a consequence of the deteriorating properties of the electron injecting Ba contact upon exposure to air. After 24 hours the conventional device has ceased functioning. This degradation is related to rapid degradation of the barium contact layer. After deposition a $BaAl_4$ alloy is formed at the interface with the polymer.[21] Upon exposure to water that penetrates through the pinholes in the Al cover layer an insulating $Al(OH)_3$ layer is formed at the interface. This layer effectively prevents electron injection and therefore kills the electroluminescence, leading

to the formation of black spots. The inverted device however maintains a high current density and light output. Since the emitting polymer layer is identical in both cases, the only conclusion is that the differences in degradation behavior are caused by the difference in contacts. Therefore the metal oxide contacts show excellent ambient stability in injecting charges, compared to the conventional contacts. Besides this quantitative difference, Fig. 5 also shows the deterioration qualitatively. Depicted are photographs of the devices operating in ambient conditions after set periods of time. Both devices were consistently captured in a single frame for equal lighting conditions, as well as being operated at the same initial current density of 10^3 A/m^2. The formation of dark areas of zero electroluminescence can clearly be seen in the conventional device, starting mere minutes after exposure to air, eventually breaking down completely after approximately 19 hours. The distinctive nucleation of these spots and their growth can evidently be seen on the photographs. In contrast, the inverted geometry device remains uniform, in agreement with the results obtained from the electrical measurements. We can therefore conclude that the spin-cast ZnO bottom cathode injects electrons efficiently into PF10TBT and also exhibits excellent air stability as compared to the commonly used thermally evaporated low work function metal electrodes.

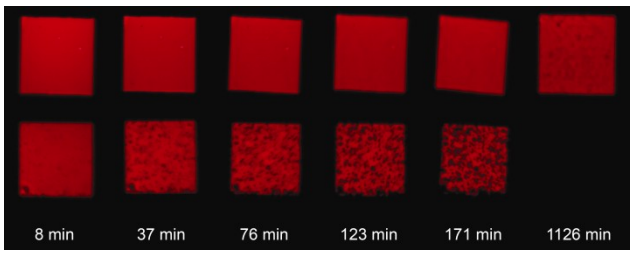

Figure 5. Digital photographs of operated devices under ambient conditions. The top row shows the inverted devices, while the bottom row shows the conventional devices.

Finally we compare the characteristics of the fully solution processed system with a spin-cast V_2O_5 anode to the reference device with the evaporated MoO_3 anode. Fig. 6a shows a comparison of the *J-V* characteristics of the two devices, as well as the *J-V* curves of the V_2O_5 based LED in its pristine state and after operation in air for approximately 92 hours in Fig. 6b. The performance of the two systems is remarkably similar. The current density is even slightly higher for the solution processed V_2O_5 device, due to a slightly

thinner polymer layer. The electrical characterization clearly shows that both materials give an ohmic hole injecting contact to the polymer highest occupied molecular orbital (HOMO). Similar stability to the evaporated

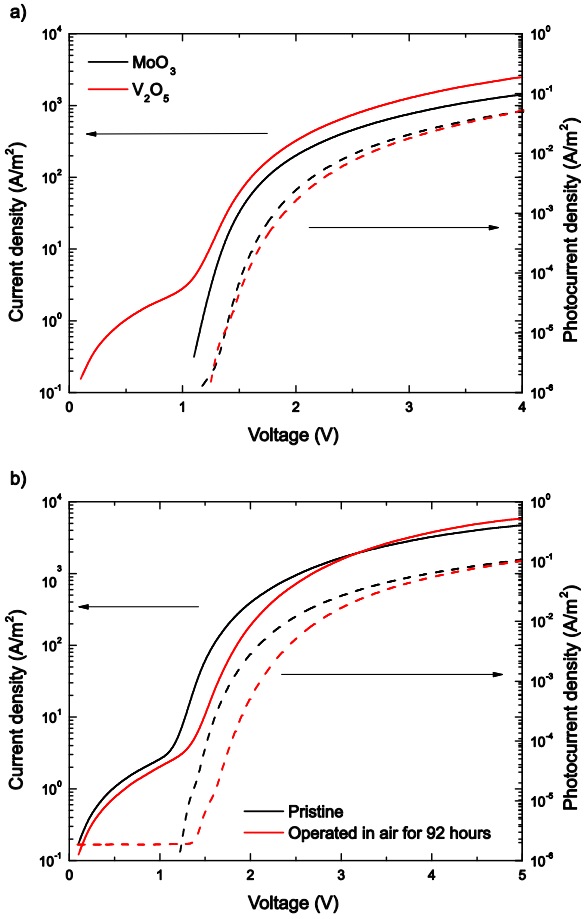

Figure 6. Performance comparison of the devices with anodes based on MoO_3 and V_2O_5. a) *J-V* and *L-V* characteristics. b) Operational stability of V_2O_5 devices, shown are curves before and after 92 hours of operation in air.

MoO_3 LED can be observed in the V_2O_5 devices, showing only little degradation after 92 hours of operation in ambient conditions, further exemplifying the excellent air stability of metal oxide materials.

4.3 Conclusions

An all-solution processed PLED with two ohmic contacts has been realized. The fact that these PLEDs are also stable in air for various hours without encapsulation is beneficial for a roll-to roll production process. It implies that the PLEDs can first be processed roll-to-roll from solution and that later on a barrier foil can be laminated to the device. Another intriguing question is what kind of requirements with regard to the water vapor transmission rate of the barrier stack are needed for this type of all-solution processed PLEDs, which is a subject of further research.

In the previous chapters the use of precursor ZnO based electron transport layers has been described. In the next chapter the use of ZnO nanoparticles as middle electrode in a tandem solar cell will be discussed.

4.4 References

1. S. Reineke, F. Lindner, G. Schwartz, N. Seidler, K. Walzer, B. Lussem, K. Leo, Nature, 459, (2009), 234-238.

2. D. de Leeuw, M. Simenon, A. Brown, R. Einerhand, Synth. Met., 87, (1997), 53-59.

3. H.J. Bolink, E. Coronado, D. Repetto, M. Sessolo, Appl. Phys. Lett., 91, (2007), 223501-223501-3.

4. K. Morii, M. Ishida, T. Takashima, T. Shimoda, Q. Wang, M.K. Nazeeruddin, M. Graetzel, Appl. Phys. Lett., 89, (2006), 183510-183510-3.

5. H.T. Nicolai, G.A.H. Wetzelaer, M. Kuik, A.J. Kronemeijer, B. de Boer, P.W.M. Blom, Appl. Phys. Lett., 96, (2010), 172107-172107-3.

6. H. You, Y. Dai, Z. Zhang, D. Ma, J. Appl. Phys., 101, (2007), 026105-3.

7. T. Matsushima, Y. Kinoshita, H. Murata, Appl. Phys. Lett., 91, (2007), 253504-3.

8. T. Matsushima, H. Murata, J. Appl. Phys., 104, (2008), 034507-034507-4.

9. H.J. Bolink, E. Coronado, D. Repetto, M. Sessolo, E.M. Barea, J. Bisquert, G. Garcia-Belmonte, J. Prochazka, L. Kavan, Adv. Funct. Mater., 18, (2008), 145-150.

10. M. Kroger, S. Hamwi, J. Meyer, T. Riedl, W. Kowalsky, A. Kahn, Appl. Phys. Lett., 95, (2009), 123301-3.

11. G. Li, C. Chu, V. Shrotriya, J. Huang, Y. Yang, Appl. Phys. Lett., 88, (2006), 253503-3.

12. V. Shrotriya, G. Li, Y. Yao, C. Chu, Y. Yang, Appl. Phys. Lett., 88, (2006), 073508-3.

13. S. Tokito, K. Noda, Y. Taga, J. Phys. D: Appl. Phys., 29, (1996), 2750.

14. K. Takanezawa, K. Tajima, K. Hashimoto, Appl. Phys. Lett., 93, (2008), 063308-063308-3.

15. W. Prandtl, L. Hess, Z. Anorg. Ch., 82, 1913103-129.

16. J. Livage, Chem. Mater., 3, (1991), 578-593.

17. J. Livage, Solid State Ionics, 86-88, (1996), 935-942.

18. T.T. Larsen-Olsen, E. Bundgaard, K.O. Sylvester-Hvid, F.C. Krebs, Org. Electron., 12, (2011), 364-371.

19. M.A. Lampert, P. Mark, Current Injection in Solids, Academic, New York (1970).

20. D.J.D. Moet, M. Lenes, J.D. Kotlarski, S.C. Veenstra, J. Sweelssen, M.M. Koetse, B. de Boer, P.W.M. Blom, Org. Electron., 10, (2009), 1275-1281.

21. C. Bulle-Lieuwma, P. van de Weijer, Appl. Surf. Sci., 252, (2006), 6597-6600.

Chapter 5

High work function transparent middle electrode for organic tandem solar cells

The use of poly(3,4-ethylenedioxythiophene) poly(styrenesulfonate) (PEDOT:PSS) in combination with ZnO as middle electrode in solution-processed organic tandem solar cells requires a pH modification of the PEDOT:PSS dispersion. It is demonstrated that this neutralization leads to a reduced work function of PEDOT:PSS, which does not affect the performance of polythiophene:fullerene solar cells, but results in a lower open-circuit voltage of devices based on a polyfluorene derivative with a higher ionization potential. The introduction of a thin layer of a perfluorinated ionomer recovers the anode work function and gives an open-circuit voltage of 1.92 V for a double junction polyfluorene-based solar cell

5.1 Introduction

An attractive route towards more efficient polymer-based photovoltaics is to combine two or more cells with complementary absorption spectra in a multijunction device. Ideally these subcells should be interconnected by a fully solution-processed, conductive and transparent middle contact. It has been demonstrated that by covering a layer of ZnO nanoparticles with a neutral pH dispersion of poly(3,4-ethylenedioxythiophene) poly(styrenesulfonate) (PEDOT:PSS), a transparent and conductive interface can be obtained. [1] In this all spin-cast tandem solar cell the front cell consisted of a blend of a poly(phenylene vinylene) derivative as electron donor and [6,6]-phenyl C_{61} butyric acid methyl ester (PCBM) as electron acceptor, whereas the back cell on top of the interconnecting ZnO/neutral PEDOT contact was made from poly(3-hexyl thiophene) (P3HT).[1] The pH modification of the PEDOT dispersion is needed to prevent the dissolving of the underlying ZnO layer. Ultraviolet photoemission spectroscopy (UPS) studies have demonstrated that an increased pH of electronic grade PEDOT:PSS by addition of NaOH results in a decrease of the work function.[2,3] For the back cell containing P3HT, with an ionization potential of 4.8 eV, it was demonstrated that the neutral PEDOT:PSS middle contact still works as an Ohmic contact. An important question, however, is whether the neutral PEDOT:PSS is still able to form an Ohmic contact on polymers having high ionization potentials, e.g., polyfluorene derivatives. If this is not the case a strong reduction of the open-circuit voltage is expected.[4]

5.2 Results and discussion

In this chapter the acidity of a highly conductive PEDOT:PSS dispersion (Clevios PH500, PEDOT:PSS ratio 1:2.5 by weight, H.C. Starck) was altered systematically by addition of a 1:8 dilution of 2-dimethylaminoethanol (DMAE, Aldrich) in water, as shown in Fig. 1 The obtained acidity ranged from pH 1.9 for unmodified PH500 to a slightly basic pH 8.5 after addition of 3.0 vol% DMAE:H_2O.

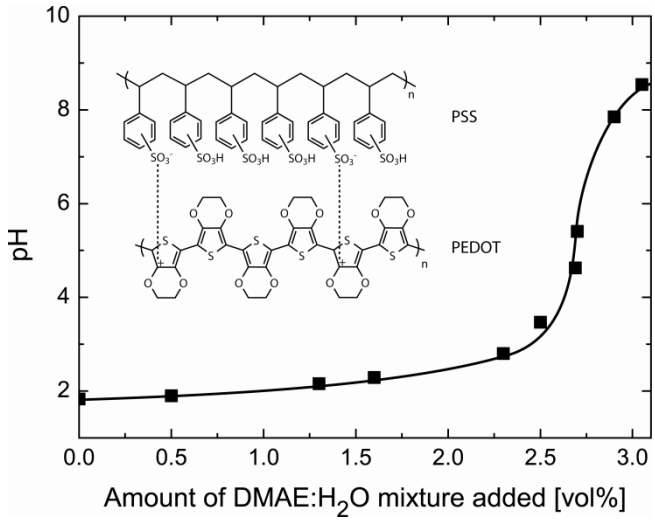

Figure 5. Titration curve of Clevios PH500 with a 1:8 dilution of DMAE in water. On the horizontal axis, the relative amount of DMAE solution added to the PEDOT:PSS dispersion is displayed. The line serves to guide the eye. The inset shows the chemical structures of PEDOT and PSS.

It is relevant to know to what extent the acidity of PEDOT:PSS should be modified in order to keep the underlying ZnO layer intact. As an indication, the UV-VIS absorbance of a pristine ZnO layer at $\lambda = 350$ nm, as measured with a Perkin-Elmer Lambda 900 spectrophotometer, was compared to the absorbance of ZnO layers on which PEDOT:PSS of varying pH was applied via spin coating. Due to dissolution in acidic PEDOT:PSS, the absorbance of ZnO strongly decreased below pH 3. Additionally, a dramatic loss in wetting quality and film formation properties of PEDOT:PSS on ZnO was observed at low pH. When applied in multilayer solar cells using ZnO, the PEDOT:PSS dispersion should therefore have a pH $\geq$ 3.

To assess the usability of the combined interlayers, we spin-cast single and double junction solar cells from an 8 mg/mL solution of P3HT:PCBM (1:1 by weight) in chloroform. The active layers of the single cell and the front subcell of the double junction device were applied on electronic grade PEDOT:PSS (Clevios VP AI4083, H.C. Starck). To form the interlayer in the double junction configuration, an 18 mg/mL acetonic dispersion of ZnO nanoparticles, synthesized as described elsewhere,[5, 6] and a modified

PH500:DMAE dispersion at pH 3.4 (hereafter referred to as PH500M) were subsequently spin-cast in air on top of the first P3HT:PCBM layer. Both interlayers were approximately 30 nm thick. One thermal annealing step of 5 min at 140 ºC was carried out in nitrogen atmosphere after all solution-processed layers were applied. A cathode consisting of 1 nm LiF and 100 nm Al was thermally deposited at ~ 10^{-6} mbar. Current-voltage characteristics were performed with a Keithley 2400 SourceMeter under illumination from a Steuernagel SolarConstant 1200 set to 1 sun intensity using a silicon refence cell and corrected for spectral mismatch (M = 1.40).[7] To eliminate time-dependent UV-effects the light was filtered with a GG385 UV filter. Contributions to the photocurrent from regions outside the test area were eliminated using illumination masks. Figure 6 shows the photovoltaic properties of the double junction solar cell: V_{oc} = 1.10 V, fill factor FF = 0.67, and short-circuit current density J_{sc} = 22.6 A/m². The single layer device showed V_{oc} = 0.55 V, FF = 0.64 and J_{sc} = 48.1 A/m². The addition of open-circuit voltages in the P3HT based double junction device and the maximum output power of 1.7 mW/cm² for both cells show that the ZnO/PH500M intermediate contact does not introduce any limitations to device performance.

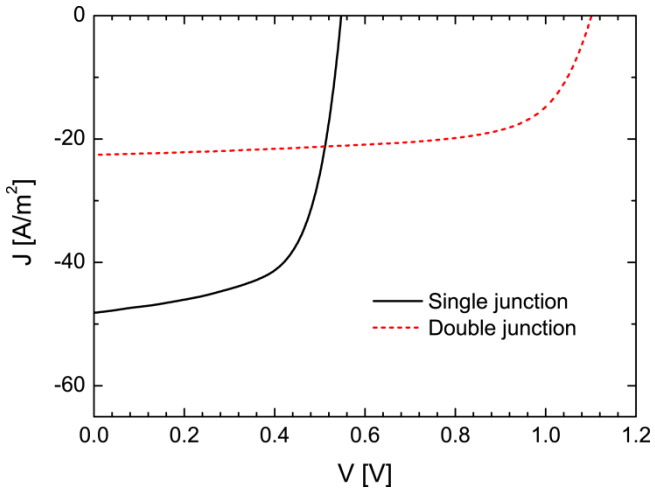

Figure 6. Current-voltage characteristics of single (solid line) and double (dashed line) junction P3HT:PCBM solar cells. The thickness of all P3HT:PCBM layers is ca. 125 nm.

As an alternative to P3HT, solar cells based on poly[9,9-didecanefluorene-alt-(bis-thienylene) benzothiadiazole] (PF10TBT) and PCBM with a power conversion efficiency of 4.2% were reported.[8] The optical band gap of PF10TBT is similar to that of P3HT, but the energy levels of the highest occupied molecular orbital (HOMO, -5.4 eV) and lowest unoccupied molecular orbital (LUMO, -3.4 eV) result in a much smaller potential loss at the donor-acceptor interface and a higher open-circuit voltage of nearly 1 V. A series-connected double junction solar cell of PF10TBT:PCBM should thus produce a V_{oc} close to 2 V. However, using the ZnO/PH500M interlayer, we found a rather large spread in V_{oc} for such devices with a maximum of only 1.5 V. This reduced V_{oc} in the PF10TBT:PCBM cells is a direct consequence of the reduced work function of PH500 after neutralization. In order to further quantify this effect, the non-destructive Kelvin probe (KP) method was used to measure the work function of layers of the series of modified PH500 dispersions with varying PH on ITO in a nitrogen atmosphere. Subsequently, an 80 nm thick layer of PF10TBT:PCBM (1:4 by weight) was spin-cast in air from a 3 mg/mL (polymer) solution in chlorobenzene, followed by thermal deposition of a LiF/Al cathode. The only intentional difference between the resulting photovoltaic devices was the acidity of the applied PH500M dispersion. The open-circuit voltage of each device was extracted from current-voltage (IV) measurements under illumination (again, M=1.40). The results of the KP and IV measurements are shown together as a function of pH in Figure 7. The work function strongly decreases with increasing pH. At pH 3.4 it has dropped by more than 0.5 eV compared to that of unmodified PH500. This is consistent with the V_{oc} loss from 2 to 1.5 V in the double junction cell made from PF10TBT:PCBM. An even further decrease of the work function is observed for higher pH. This demonstrates that the open-circuit voltage of PF10TBT:PCBM cells is reduced markedly by the pH-induced work function change. As a result the ZnO/PH500M middle electrode is only suited in combination with top cells with a donor of which the HOMO levels are located around 4.8-4.9 eV, as P3HT.

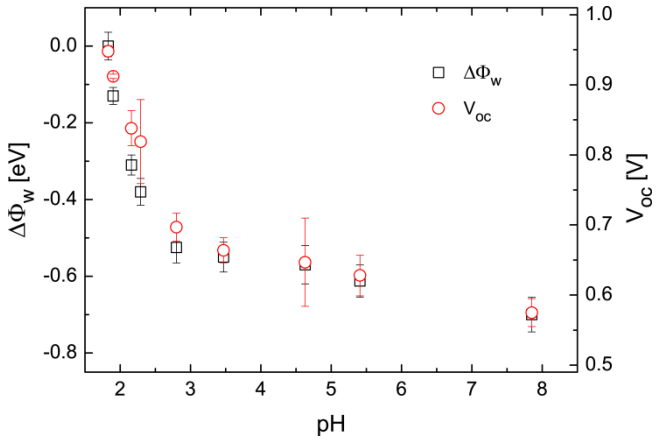

Figure 7. Squares: pH-induced work function decrease of 45 nm thick PH500M layers on top of ITO. Circles: open-circuit voltage of PF10TBT:PCBM single junction cells processed on the same ITO/PH500M substrates.

In order for the back cell to produce the expected photovoltage, a method is needed to recover the work function of the back cell anode. Electronic grade PEDOT:PSS can be reformulated by addition of a 5 wt% Nafion® perfluorinated resin solution in a water/alcohol mixture (Aldrich) to obtain a work function of 5.7 eV.[9] Addition of a Nafion solution to pH modified PEDOT:PSS dispersions is considered less feasible, since it introduces an additional acidic component to the formulation. It is, however, possible to apply a thin Nafion-only layer that raises the work function of the underlying anode. Lee *et al.* have reported that the work function of ITO increases by 0.5 eV when covered with a thin Nafion layer.[10] Moreover, using density-functional theory (DFT) calculations, they showed that the ionization potentials of Nafion-like compounds are systematically higher than those of polystyrene sulfonic acids. Here, we incorporate an interfacial layer of Nafion in a double junction solar cell of PF10TBT:PCBM, by spin coating Nafion perfluorinated resin solution, highly diluted in ethanol, on top of the PH500M (pH 3.4) anode before applying the second photoactive layer. An Ohmic hole contact between PH500M and PF10TBT has now been restored, without compromising the compatibility with the underlying ZnO layer.

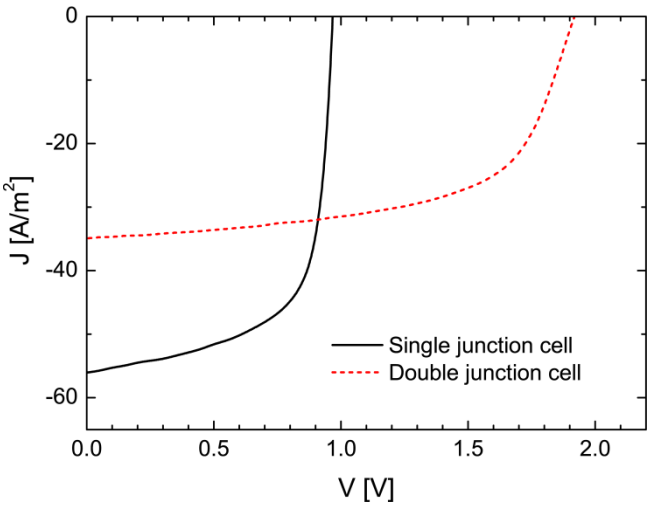

Figure 8. Current-voltage characteristics of single (solid line) and double (dashed line) junction PF10TBT:PCBM solar cells. The two subcells were interconnected with ZnO/PH500M/Nafion interlayers. The thickness of all PF10TBT:PCBM layers is ca. 80 nm.

As shown in Figure 8, this method results in a well-performing double junction PF10TBT:PCBM solar cell with V_{oc} = 1.92 V, FF = 0.61 and J_{sc} = 34.9 A/m². The single junction device, processed on electronic grade PEDOT:PSS, has V_{oc} = 0.98 V, FF = 0.66 and J_{sc} = 56.0 A/m². These results are summarized in Table 2. Now, due to the inclusion of a thin layer of Nafion, the double junction cell has an open-circuit voltage virtually twice as high as the single junction device. Altogether, the maximum output power of the double junction cell of 4.1 mW/cm² is higher than that of the optimized single layer cell (3.6 mW/cm²). The physical origin of this effect will be discussed elsewhere.

Active layer(s)	Type	Jsc [A m^{-2}]	V_{oc} [V]	FF [%]	MPP [mW cm^{-2}]
P3HT:PCBM	Single junction	48.1	0.55	64	1.7
	Tandem	22.6	1.10	67	1.7
PF10TBT:PCBM	Single junction	56.0	0.98	66	3.6
	Tandem	34.9	1.92	61	4.1

Table 2. Photovoltaic performance of single junction and tandem cells based on P3HT:PCBM and PF10TBT:PCBM layers under white light illumination at ~ 0.9 sun intensity.

5.3 Conclusions

In conclusion, the acidity of PEDOT:PSS has been modified to evaluate its use in multilayer polymer solar cells containing interlayers of ZnO nanoparticles. By addition of DMAE, the pH was varied from 1.9 to 8.5. The dispersions are compatible with ZnO for pH ≥ 3. Addition of open-circuit voltage and preservation of fill factor were demonstrated for a double junction P3HT:PCBM solar cell. The reduction of the work function of PEDOT:PSS upon neutralization, exceeding more than 0.5 eV, was shown to cause lower open-circuit voltages in polyfluorene-based cells with a higher ionization potential. An Ohmic hole contact was restored by inclusion of a thin layer of Nafion, which enabled the fabrication of double junction PF10TBT:PCBM cells with a V_{oc} as high as 1.92 V.

5.4 References

1. J. Gilot, M. M. Wienk and R. A. J. Janssen, *Appl. Phys. Lett.* 90, (2007), 143512.

2. M. M. de Kok, M. Buechel, S. I. E. Vulto, P. van de Weijer, E. A. Meulenkamp, S. H. P. M. de Winter, A. J. G. Mank, H. J. M. Vorstenbosch, C. H. L. Weijtens and V. van Elsbergen, *Phys. Stat. Sol. A* 201, (2004), 1342.

3. C. H. L. Weijtens, V. van Elsbergen, M. M. de Kok and S. H. P. M. de Winter, *Org. Electron.* 6, (2005), 97.

4. V. D. Mihailetchi, P. W. M. Blom, J. C. Hummelen and M. T. Rispens, *J. Appl. Phys.* 94, (2003), 6849.

5. C. Pacholski, A. Kornowski and H. Weller, *Angew. Chem. Int. Ed.* 41, (2002), 1188.

6. W. J. E. Beek, M. M. Wienk, M. Kemerink, X. N. Yang and R. A. J. Janssen, *J. Phys. Chem. B* 109, (2005), 9505.

7. J. M. Kroon, M. M. Wienk, W. J. H. Verhees and J. C. Hummelen, *Thin Solid Films* 403-404, (2002), 223.

8. L. H. Slooff, S. C. Veenstra, J. M. Kroon, D. J. D. Moet, J. Sweelssen and M. M. Koetse, *Appl. Phys. Lett.* 90, (2007), 143506.

9. T.-W. Lee, O. Kwon, M.-G. Kim, S. H. Park, J. Chung, S. Y. Kim, Y. Chung, J.-Y. Park, E. Han, D. H. Huh, J.-J. Park and L. Pu, *Appl. Phys. Lett.* 87, (2005), 231106.

10. T.-W. Lee, Y. Chung, O. Kwon and J. J. Park, *Adv. Funct. Mater.* 17, (2007), 390.

Chapter 6

Diffusion-Limited Current in Organic Metal-Insulator-Metal Diodes

Engineering of contacts and work function is important to optimize and understand the operation of organic devices. Typically, organic solar cells and light-emitting diodes make use of contacts with different work functions to efficiently inject or extract charge carriers. Due to the work function difference these devices exhibit a built-in voltage. For applied voltages lower than the built-in voltage the electric field is opposite to the direction of the current. In this case the current is dominated by diffusion of charge carriers. In this chapter, an analytical expression for the diffusion current in organic metal-insulator-metal diodes is derived. The derivation is based on the classical diffusion theory of Schottky, with adaptations to account for the absence of doping, a built-in voltage due to asymmetric contacts, and band bending at the Ohmic contact. The commonly observed deviation of the ideality factor from unity (~1.2) is characteristic of diffusion-limited currents in undoped organic semiconductors. Summing with the classical space-charge limited current provides a full analytic description of the current as a function of voltage, temperature and layer thickness.

6.1 Introduction

Conjugated polymers and small molecules, as typically used in organic light-emitting diodes or solar cells are undoped semiconductors. When these semiconductors are sandwiched between two electrodes, a metal-insulator-metal (MIM) diode stack is formed. Many organic diodes consist of an Ohmic injecting contact and a non-Ohmic collection contact. In general, when electrodes with different work function are used an internal electric field will build up resulting in a built-in voltage V_{bi} across the undoped semiconductor, which equals the difference in work function of the electrodes.

6.2 Theory

As a reference, we consider the case of a hole-only MIM diode with one Ohmic and one non-Ohmic contact, as shown in Fig. 1a. The collecting contact at $x=L$, where x denotes the position within the diode and L is the film thickness, is separated from the valence band by a barrier height, φ_b. The injecting contact at $x=0$ aligns with the valence band. For both contacts the energy barrier to the conduction band is so large that electron injection can be neglected. The built-in voltage V_{bi} is then equal to the barrier height φ_b. At high positive bias on the Ohmic contact, larger than the built-in voltage, the resulting electric field becomes positive, pointing towards the collecting contact. Holes are injected and the current is dominated by drift. The current becomes limited by the uncompensated charges of the injected holes, leading to a space-charge-limited current (SCLC) that can be analytically described by the Mott-Gurney equation[1] as

$$J = \frac{9}{8}\varepsilon\mu\frac{(V-V_{bi})^2}{L^3}, \qquad (1)$$

with ε the dielectric constant, μ the charge-carrier mobility, and V the applied voltage. A large advantage of such an analytical description is that from experimental data on single-carrier devices the charge carrier mobility can directly be obtained from current density versus voltage (J-V) measurements[2].

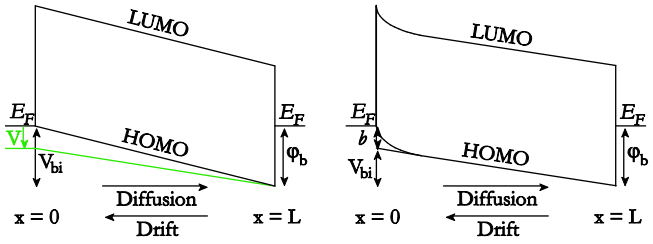

Figure 1. Energy-band diagram of an organic hole-only MIM diode. The layer thickness is *L*. *x* denotes the position in the diode. The contact at x = 0 is Ohmic, while the collecting contact at *x*=*L* is separated from the valence band by a barrier height φ_b. (a) thermal equilibrium (black) and upon applying a small positive bias smaller than the built-in voltage (green). (b) band diagram at thermal equilibrium by including band bending due to injected holes at the Ohmic contact.

As shown in Fig. 1a, we now apply a small positive bias on the injecting contact. When the bias is smaller than the built-in voltage the electric field is still negative, pointing towards the injecting contact. The drift current due to the injected holes is therefore negative. However, the gradient in the hole density leads to diffusion of holes towards the collecting contact. The net positive current then results from the positive diffusion current that dominates over the negative drift current.

Until now the diffusion-limited current in organic MIM diodes has been analyzed using the classical Shockley diode equation[3], given by

$$J = J_0\left[\exp\left(\frac{qV}{\eta kT}\right)-1\right], \qquad (2)$$

where J_0 is normally taken as a fit parameter, and η an empirical ideality factor. However, Eq. (2) was derived to describe a bipolar current through a *p-n* diode, where the ideality factor is strictly related to the order of recombination. Applying this equation to unipolar devices with undoped semiconductors is therefore questionable, but nevertheless frequently used in these cases. It was recently demonstrated that in organic MIM diodes this ideality factor deviates from unity by the presence of energetically deep states within the band gap[4]. However, a remarkable result was that even for organic semiconductors such as poly(9,9-dioctylfluorene) (PFO), the poly(*p*-phenylene vinylene) (PPV) derivative BEH/BB-PPV and the fullerene derivative PCBM that all show non-dispersive transport, pointing to the absence of deep traps, an ideality factor of typically 1.2 was found instead of unity.

In this Chapter, an analytical equation is derived that describes the diffusion current for undoped semiconductors or insulators in MIM diodes with asymmetric contacts. The derivation is based on the classical diffusion model put forth by Schottky[5] for a metal contact on a doped inorganic semiconductor. It is shown that the derived equation provides a simple and fast method to model diffusion currents in MIM diodes with different contacts. The analytical diffusion model allows for a direct determination of the built-in potential in organic MIM devices, which we verify on hybrid organic light-emitting diodes (HyLEDs)[6-9] with metal-oxide contacts, which are governed by universal energy alignment[10]. By summing the contributions of drift and diffusion we can now analytically describe the current through the MIM diode in the full voltage range, allowing disentanglement of the drift and diffusion contributions to the current.

The original diffusion-theory by Schottky[5] describes the situation for a metal contact on a *doped* semiconductor. In such a Schottky diode, majority carriers diffuse from the semiconductor into the metal to equilibrate the Fermi level. The charge of the remaining uncompensated dopants then leads to the build-up of an electric field in the depletion region, resulting in band bending. A similar model was used by Shockley for the current across a *p-n* junction, *viz.* a depletion region formed between a *p*- and *n*-doped semiconductor[3]. An alternative theory to describe the current in a Schottky diode, based on thermionic emission, is valid only for high charge-carrier mobilities[11,12], whereas diffusion is the limiting case in low-mobility semiconductors, like organic semiconductors.

In MIM structures, band bending due to uncompensated dopants is absent. Below we will introduce the appropriate boundary conditions[13]. We start with the hole-only MIM diode of Fig. 1a. Following the classical derivation of Schottky for diffusion currents the hole current density is given by

$$J_p = \mu_p kT\left(\frac{p}{kT}\frac{dE_v}{dx} - \frac{dp}{dx}\right), \tag{3}$$

where the diffusion coefficient has been replaced by the mobility μ_p through the Einstein relation[4]. However, in contrast to a Schottky diode, the limit for integration in the MIM structure has to be set to the total device thickness L, since the device is fully depleted, leading to

$$J_p \int_0^L \exp\left(-\frac{E_v(x)}{kT}\right)dx = -\mu_p kTp(x)\exp\left(-\frac{E_v(x)}{kT}\right)\Bigg|_0^L, \quad (4)$$

with p the hole density and E_v the valence-band edge, or, analogously in this case the highest occupied molecular orbital (HOMO) of the polymer. To evaluate this expression we need to introduce the MIM boundary conditions for the charge carrier density $p(x)$ and the valence band $E_v(x)$ at the electrode-semiconductor interfaces $x=0$ and $x=L$.

As shown in Fig.1a the built-in voltage V_{bi} for this device is equal to φ_b. In that particular case the boundary conditions for the charge-carrier density at the electrodes of a metal-insulator-metal device are given by[13]

$$p(0) = N_v, \quad (5a)$$

$$p(L) = N_v \exp\left(-\frac{q\varphi_b}{kT}\right), \quad (5b)$$

whereas the boundary conditions for the valence band, with respect to the Fermi level of the hole-extraction contact, for $V<V_{bi}$ are given by

$$E_v(0) = -qV, \quad (6a)$$

$$E_v(L) = -q\varphi_b. \quad (6b)$$

Note that in this case a positive forward bias V at $x=0$ lowers the internal voltage to φ_b-V, leading to a reduction of the negative drift current of holes towards the injecting contact at $x=0$, which results in an enhanced positive current in the x-direction. Combination with Eq. (4) gives for the current

$$J_p = N_v \mu_p kT\left[\exp\left(\frac{qV}{kT}\right)-1\right]\Bigg/\int_0^L \exp\left(-\frac{E_v(x)}{kT}\right)dx. \quad (7)$$

Due to the absence of space charge there is no band bending in the MIM structure, so the positional dependence of the valence band $E_v(x)$ is just a simple triangular shape, given by

$$E_v(x) = -q\left(V + \frac{(\varphi_b - V)x}{L}\right), \quad (8)$$

yielding:

$$\int_0^L \exp\left(-\frac{E_v(x)}{kT}\right)dx = \frac{LkT}{q(\varphi_b - V)}\left[\exp\left(\frac{q\varphi_b}{kT}\right)-\exp\left(\frac{qV}{kT}\right)\right] \quad (9)$$

Substituting Eq. (9) into Eq. (7) then leads to an analytical current density expression for the diffusion-limited current in a MIM diode, given by

$$J_p = \frac{q\mu_p N_v(\varphi_b - V)\left[\exp\left(\frac{qV}{kT}\right)-1\right]}{L\left[\exp\left(\frac{q\varphi_b}{kT}\right)-\exp\left(\frac{qV}{kT}\right)\right]}. \tag{10}$$

A similar expression was obtained by Paasch *et al.* [14]. We note that the use of a constant mobility in our derivation is valid since in the diffusion regime the carrier densities in the diode are sufficiently low such that mobility enhancement due to DOS filling[15] does not play a role[16]. Before comparing Eq. (10) to experimental data it is essential to consider that for Ohmic contacts on insulators or undoped semiconductors charge carriers diffuse from the electrode into the semiconductor, forming an accumulation region close to the contact[17]. As shown in Fig. 1b the accumulated charge carriers close to the injecting contact at $x=0$ cause band bending and reduce the built-in voltage of the device. Reported values for this band bending, here described by the parameter b, typically lie in the range of 0.2-0.3 V and depend also on energetic disorder.[18-22] To account for this accumulation we approximate the energy band diagram of the MIM diode by the dashed lines in Fig. 1b. In this way the reduction of the built-in voltage is taken into account, while maintaining the triangular potential. Then the boundary conditions are modified to

$$p(0) = N_v \exp\left(-\frac{qb}{kT}\right), \tag{11a}$$

$$p(L) = N_v \exp\left(-\frac{q\varphi_b}{kT}\right), \tag{11b}$$

$$E_v(0) = -q(V+b), \tag{11c}$$

$$E_v(L) = -q\varphi_b. \tag{11d}$$

The current equation, Eq. (10), is for this case modified to

$$J_p = \frac{q\mu_p N_v(\varphi_b - b - V)\left[\exp\left(\frac{qV}{kT}\right)-1\right]}{L\exp\left(\frac{qb}{kT}\right)\left[\exp\left(\frac{q(\varphi_b - b)}{kT}\right)-\exp\left(\frac{qV}{kT}\right)\right]}. \tag{12}$$

Clearly, the band-bending parameter b does not only reduce the built-in voltage, but also has a large impact on the current close to the V_{bi} and above V_{bi}. Therefore, we introduce the band-bending parameter b according to

$$b = \frac{kT}{q}\left[\ln\left(\frac{q^2 N_v L^2}{2kT\varepsilon}\right) - 2\right], \tag{13}$$

based on a model by Simmons[18]. At V_{bi}, the current undergoes a transition from an exponential to a linear dependence on voltage. Due to the thickness dependence of the band-bending parameter, the linear current above V_{bi} depends inversely on L^3, while the exponential part below V_{bi} scales inversely with L. For voltages larger than the built-in voltage, the electric field becomes positive and the drift current starts to dominate. This is the well-known space-charge-limited current, described by Eq. (1). With the derived diffusion current, Eq. (12), we can now obtain the complete current through the device by summing the contributions of drift and diffusion, as shown in Fig. 2. The drift current starts exactly at the built-in voltage, well defined by φ_b-b. The analytical expression for the diffusion current now allows disentanglement of the drift and diffusion contributions to the current.

When comparing the expression for the diffusion-limited current for MIM diodes, Eq. (12), to the classical Shockley diode equation, Eq. (2), it is clear that there are subtle differences in the voltage dependence of the current density, as shown in the inset of Fig. 2. In order to match the slope of Eq. (12) using an effective barrier, φ_b-b, of 0.3 V, the ideality factor in Eq. (2) has to be adjusted to 1.2. This explains why experimentally in organic semiconductors without deep traps small deviations from unity of the ideality factor of about 0.2 were found when the Shockley equation was used for the analysis. This slight deviation from unity is therefore a fundamental property of organic MIM diodes, related to the charge transport. We note that the exact value of the deviation depends on the value of the effective applied voltage, φ_b-b-V. For most organic MIM diodes, the ideality factor is determined within 0.3 V below the built-in voltage (φ_b-b)[4], leading to an apparent ideality factor of ~1.2. For large barriers, carriers of the opposite sign will be injected, leading to trap-assisted recombination that will enhance the ideality factor.[23]

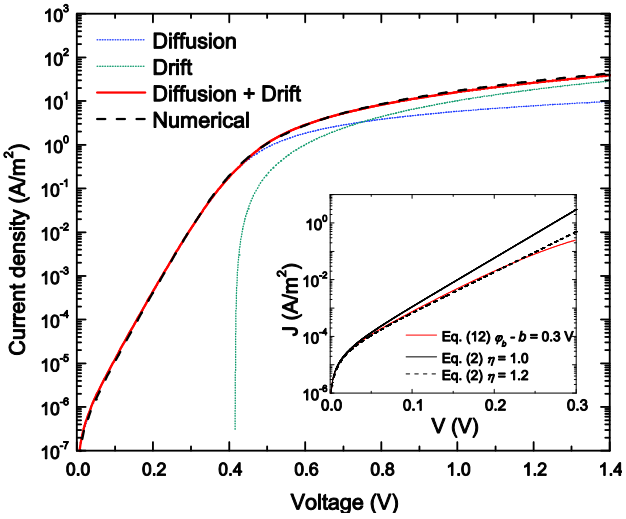

Figure 2. Current density-voltage characteristics for a device with φ_b=0.7 V, μ_p=1×10^{-9} m^2/Vs, N_v=3×10^{26} m^{-3}, L=100 nm, T=295 K, and ε=3ε_0. The dotted and solid lines are the analytically calculated characteristics for diffusion, drift, and the sum of drift and diffusion. The dashed line represents a numerical simulation [11] with the exactly the same parameters. The inset shows a comparison between the calculated current for a MIM diode, Eq. (12), with φ_b-b=0.3 V (red line) and the current calculated with the classical Shockley equation using an ideality factor of unity (solid black line). A good approximation is obtained using an ideality factor of 1.2 (dashed line).

6.3 Results

To evaluate the applicability of the expression derived for the diffusion-limited current in MIM diodes we investigated a PFO hole-only diode with PEDOT:PSS and MoO_3 contacts. MoO_3 provides an Ohmic contact even to PFO with a HOMO as deep as 5.8 eV.[24] The work function of PEDOT:PSS is around 5.2 eV. Hence PEDOT:PSS serves as the collecting contact with an estimated energy barrier of about 0.6 eV. The exact value is not a priori known and may depend on the presence of interface dipoles and on Fermi level pinning due to interface trap states.

The experimental temperature-dependent current-voltage characteristics are shown in Fig. 3. At low bias the current increases exponentially with bias as expected for a diffusion-limited current. Above about 0.4-0.5 V the current becomes drift-dominated and limited by the uncompensated charges of the injected holes, leading to a space-charge-limited current.

The parameters describing the charge-carrier mobility of PFO as a function of carrier density and temperature are well known.[24] The diffusion-limited current can now be fitted to the experimental data by adjusting the barrier in Eq. (12). The solid lines are a fit to the experimental data. A good agreement in the diffusion regime at $V<V_{bi}$ is obtained using a barrier φ_b of 0.67 V, with a band-bending parameter of 0.26 V (Eq. (13)). The value for the barrier corresponds to previous estimates of the energy barrier between PFO and PEDOT:PSS of about 0.6 eV.[24]

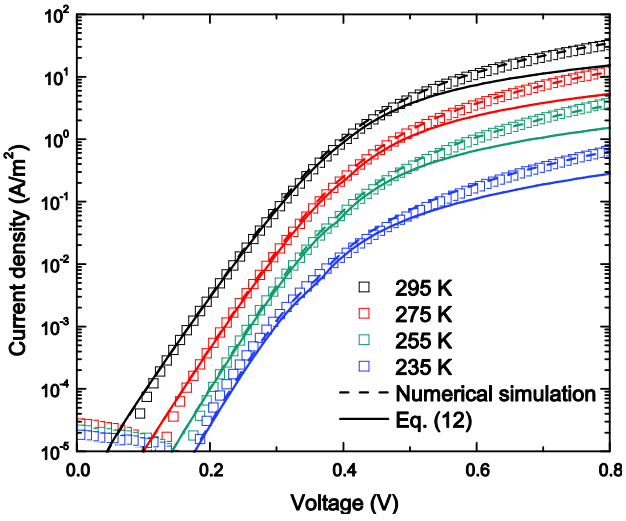

Figure 3. Current-voltage characteristics of a PEDOT:PSS/PFO(80 nm)/MoO_3 hole-only MIM diode. PEDOT:PSS is grounded. The solid lines are fits to the experimental data (symbols) using the analytical equation for the diffusion-limited current. The deviation at higher voltages is due to the current being dominated by the drift term (SCLC, Eq. (1)) above the built-in voltage. The dashed lines represent numerical device calculations using a drift-diffusion solver [13] with exactly the same parameters as extracted from the analytical description.

The dashed lines in Fig. 3 represent numerical device calculations using a drift-diffusion solver [13], with exactly the same parameters as used in the analytical fits. The numerical simulation contains both drift and diffusion, and band-bending at the injecting contact is taken implicitly into account. The good agreement verifies the analytical expression of the diffusion-limited current in an organic MIM diode. The deviations for $V>V_{bi}$ are due to the current being dominated by the drift term at those voltages.

With the *b* parameter known, the analytical description for the diffusion-limited current in MIM diodes can be used to accurately determine the built-in voltage and injection barrier of the collecting contact. As an example we investigated hole-only diodes of the polymers poly[3-hexylthiophene] (P3HT), poly[2-methoxy-5-(2-ethylhexyloxy)-1,4-phenylenevinylene] (MEH-PPV), and PFO with oxidic electrodes. MoO_3 was used as an Ohmic hole-injecting contact. ZnO is used as collecting contact. The work function of ZnO is about 4.0 eV. Taken into account the reported HOMO energies of -4.8 eV, -5.1 eV and -5.8 eV this then yields expected energy barriers of 0.8 eV, 1.1 eV and 1.8 eV for P3HT, MEH-PPV, and PFO, respectively.

The current-voltage characteristics are presented in Fig. 4. At very low bias, the current is below the detection limit of the measurement setup. With increasing bias, the exponential diffusion current exceeds the noise level. The solid lines represent fits of the diffusion-limited current in MIM diodes to the experimental data. The values for the barriers extracted are 0.93 V, 1.15 V, and 2.35 V. The obtained barriers agree well with the estimated energy barriers. This observation confirms the previous findings that the electron chemical potential is the main driving force for energy-level alignment at contacts consisting of an organic semiconductor and transition-metal oxides.[10]

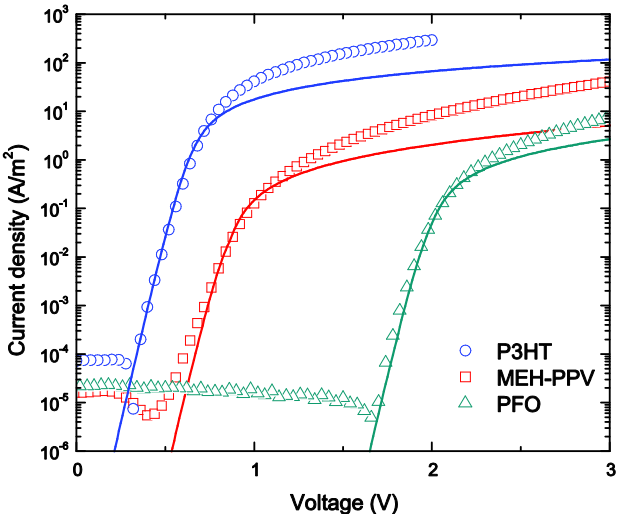

Figure 4. Experimental current-voltage characteristics (symbols) of organic MIM diodes with an Ohmic MoO_3 contact and a ZnO collecting contact. The P3HT, MEH-PPV, and PFO layer thicknesses are 125 nm, 120 nm, and 180 nm. The solid lines are fits with Eq. (12).

6.4 Conclusions

An analytical approach to model the diffusion current in organic metal-insulator-metal diodes with one Ohmic and one non-Ohmic contact is presented. The analytical model accurately describes the voltage, temperature, and thickness dependence of the diffusion current and thus allows disentanglement of the drift and diffusion contributions to the current. This can substantially improve the accuracy of charge-transport measurements in organic-semiconductor diodes. The slight deviation of the apparent ideality factor from unity is characteristic of organic MIM diodes. Applying the analytic equation to experimental data provides an easy and accurate way of determining the built-in voltage and injection barrier in organic MIM diodes. Knowledge of the injection barrier from the diffusion current in forward bias is then an important ingredient for modeling of the injection-limited current in reverse bias, which is a subject of future study. In the next chapter the model will be further evaluated to study injection-limited currents in organic semiconductors.

6.5 References

1. S. N. F. Mott and R. W. Gurney, *Electronic Processes in Ionic Crystals* (Dover Publications, 1964).
2. P. W. M. Blom, M. J. M. de Jong, and S. Breedijk, *Appl. Phys. Lett.* 71, (1997), 930.
3. W. Shockley, *Bell Syst. Tech. J.* **28**, 435 (1949).
4. G. A. H. Wetzelaer, L. J. A. Koster, and P. W. M. Blom, Phys. Rev. Lett. 107, (2011), 066605.
5. W. Schottky, *Naturwissenschaften* **26**, (1938), 843.
6. H. J. Bolink, E. Coronado, D. Repetto, and M. Sessolo, *Appl. Phys. Lett.* 91, (2007), 223501.
7. K. Morii, M. Ishida, T. Takashima, T. Shimoda, Q. Wang, M. K. Nazeeruddin, and M. Graetzel, *Appl. Phys. Lett.* 89, (2006), 183510.
8. D. Kabra, L. P. Lu, M. H. Song, H. J. Snaith, and R. H. Friend, *Adv. Mater.* 22, (2010), 3194.
9. P. de Bruyn, D. J. D. Moet, and P. W. M. Blom, *Org. Electron.* 13, (2012), 1023.
10. M. T. Greiner, M. G. Helander, W.-M. Tang, Z.-B. Wang, J. Qiu, and Z.-H. Lu, *Nat. Mater.* 11, (2012), 76.
11. J. G. Simmons, Phys. Rev. Lett. 15, 967 (1965).
12. S. M. Sze, Physics of Semiconductor Devices (Wiley-Interscience, New York, 1981).
13. L. J. A. Koster, E. C. P. Smits, V. D. Mihailetchi, and P. W. M. Blom, *Phys. Rev. B* 72, (2005), 085205.
14. P. H. Nguyen, S. Scheinert, S. Berleb, W. Brütting, G. Paasch, *Org. Electron.* 2, (2001), 105.
15. M. C. J. M. Vissenberg and M. Matters, *Phys. Rev. B* 57, (1998), 12964.

16. W. F. Pasveer, J. Cottaar, C. Tanase, R. Coehoorn, P. A. Bobbert, P. W. M. Blom, D. M. de Leeuw and M. A. J. Michels, *Phys. Rev. Lett.* 94, (2005), 206601.

17. N. I. Craciun, J. J. Brondijk, and P. W. M. Blom, *Phys. Rev. B* 77, (2008), 035206.

18. J. G. Simmons, *J. Phys. Chem. Solids* 32, (1971), 1987.

19. V. D. Mihailetchi, P. W. M. Blom, J. C. Hummelen, and M. T. Rispens, *J. Appl. Phys.* 94, (2003), 6849.

20. J. Hwang, E. G. Kim, J. Liu, J.-L. Bredas, A. Duggal, and A. Kahn, *J. Phys. Chem. C* 111, (2007), 1378.

21. J. C. Blakesley and N. C. Greenham, *J. Appl. Phys.* 106, (2009), 034507.
22. I. Lange, J. C. Blakesley, J. Frisch, A. Vollmer, N. Koch, and D. Neher, *Phys. Rev. Lett.* 106, (2011), 216402.
23. G. A. H. Wetzelaer, M. Kuik, H. T. Nicolai, and P. W. M. Blom, *Phys. Rev. B* 83, (2011), 165204.

24. H. T. Nicolai, G. A. H. Wetzelaer, M. Kuik, A. J. Kronemeijer, B. de Boer, and P. W. M. Blom, *Appl. Phys. Lett.* 96, (2010), 172107.

Chapter 7

Injection-limited currents in organic semiconducting devices

Proper understanding of charge injection in organic semiconductor devices is vital for understanding and optimizing device performance. In this Chapter we derive an analytical equation to describe injection limited currents in organic semiconductor devices. The derivation is based on a recently developed model for the diffusion current in said devices. Using this formalism the injected current across an energetic barrier can be calculated by incorporating an expression to account for the probability of creating a low energy injection pathway in the disordered semiconductor. We show the applicability of this formalism on a benchmark conjugated polymer system before using it to explain the luminescent efficiency of organic light-emitting diodes with a non-ohmic electron contact.

7.1 Introduction

The classical theories of charge injection[1–4] have proven their merits time and again in the realm of inorganic semiconductor physics. Initial efforts to apply the same rigorous treatments to organic semiconductor devices have not produced a conclusive description of all experimental data because of the disordered nature of organic semiconductors.[5] The broad distribution of the density of states and the hopping nature of conduction make the assignment of a barrier height a complicated problem. Furthermore the electric field dependence of the injection current into such a broad distribution would require additional treatment. Previous attempts at analyzing injection currents have tried to take the disordered nature of organic materials into account and managed to reproduce some, but not all of the dependencies on device parameters found in literature.[6] Here we show that when the appropriate boundary conditions are taken into account and the disordered nature of the organic semiconductor is properly considered, it is possible to describe injection limited currents in organic semiconductors in the framework of the classical charge-carrier diffusion theory.

7.2 Theory

In Chapter 6 we showed that the diffusion current density in organic semiconductor devices can be described by considering the classical diffusion theory and introducing boundary conditions specific for metal-insulator-metal (MIM) structures. As such, the current density due to charge carrier diffusion in these devices can be expressed as (Chapter 6, equation 12):

$$J_p = \frac{q\mu_p N_v(\varphi_b - b - V)(e^{\frac{qV}{kT}} - 1)}{Le^{\frac{qb}{kT}}(e^{\frac{q(\varphi_b - b)}{kT}} - e^{\frac{qV}{kT}})} \quad (1)$$

Where N is the density of states at the band edge, μ the charge carrier mobility, b the band bending at the ohmic contacts, set to 0.18 eV per contact (chapter 6, equation 13)[7,8], L the device thickness and ϕ_b the internal potential. All other symbols have their usual meaning. As figure 1 illustrates, this should also allow us to determine the current density that can be injected across the barrier at negative bias, since in this configuration the internal potential for the

diffusion current density J_D from the ohmic contact will immediately give the barrier for charge carrier injection from the non-ohmic contact.

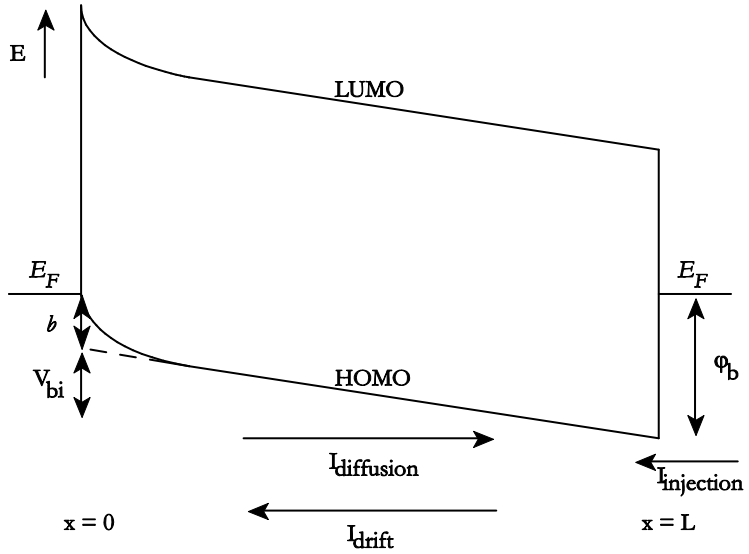

Figure 9. Band structure of a MIM device with one ohmic and one non-ohmic contact. $I_{diffusion}$ and $I_{injection}$ denote diffusion and injection currents respectively.

However, when considering charge injection into a disordered semiconductor with a broad density of states the exact barrier height is hard to determine. In 2003 Burin and Ratner theoretically considered the probability of creating a low energy injection pathway in disordered semiconductors with a non-ohmic contact.[9] Their derivations accounted for either a Gaussian or exponentially distributed density of states in the semiconductor. They arrived at an expression for a field dependent barrier lowering due to disorder. For a Gaussian density of states however an analytical solution could only be obtained under the assumption of very high electric field strength. A low-field approximation of the barrier lowering due to disorder in a material with a Gaussian density of states can be described as follows. We start from equation 44 in ref 9:

$$0 = \frac{1}{k_B T} - \frac{3\left(\varphi_* + \frac{eEa}{2}\right)^2}{6w^2 eEa} - \frac{1}{eEa} ln\left(\frac{\sqrt{2\pi}\varphi_*}{w}\right) \quad (2)$$

Figure 2a shows the numerically calculated solution to this equation (symbols) along with the high-field approximation given by eq. 45 in ref 9 (blue line). The red line gives a low-field approximation, given by:

$$\phi_d = \frac{\sigma}{4\pi}\left(\frac{qVa}{dkT}\right)^2 + \frac{\sigma}{16}. \tag{3}$$

To assess the range of applicability of this approximation, the parameters representing the temperature 'T', width of the DOS 'σ' and intersite distance 'a' were varied and the approximation compared to the numerically calculated result of eq.2. Figures 2b-2d show variation of these parameters across ranges commonly encountered in disordered organic materials. It can be seen that the approximation is excellent up until electric fields of about $6*10^7$ V/m, a sufficient range to describe the operating range of commonplace organic devices such as solar cells and light-emitting diodes. Equation 2 can then be used to express the field-dependent barrier lowering due to the disordered nature of the material.

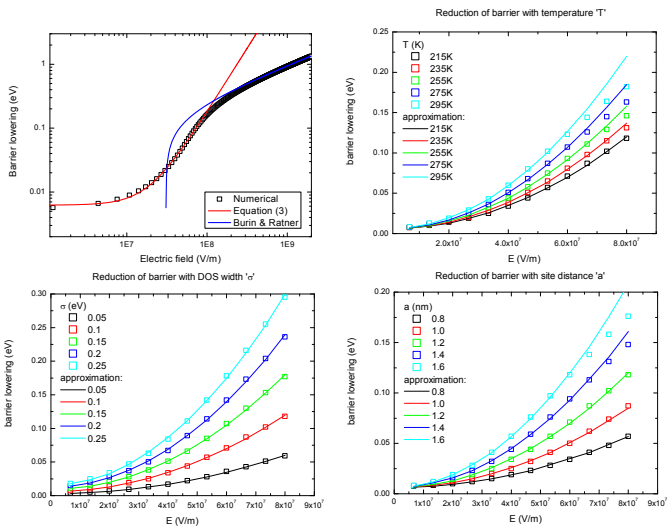

Figure 10. Comparison of high field[9] and low field (eq.3) approximations to the numerical solution to eq.2 (a) and evaluation of the parameters '*T*', '*σ*' and '*a*' governing the analytical approximation (b-d).

Furthermore, we account for the image-charge potential that will arise at the barrier contact. Therefore we employ the well-known equation for the barrier lowering due to the image charge potential:

$$\phi_i = \sqrt{\frac{qV}{4\pi\varepsilon d}} \tag{4}$$

The electric field is expressed here as V/d, since the charge carrier densities in a device with an appreciable injection barrier are sufficiently low for the electric field to be considered uniform. Furthermore, since the occupation of energy levels in the Gaussian density of states scales with $(1/2)\ (\sigma^2/kT)$,[10,11] one also has to adjust the barrier height. This leads to the last term in the expression for the barrier height:

$$\phi_t = \frac{1}{2}\frac{\sigma^2}{kT} \tag{5}$$

Combining eq. 1, 2, 3 and 4, and using negative bias for the injection current across this barrier, we can write the injection limited current for V < 0 as:

$$J_{injection} = \frac{q\mu_p N_v(\varphi_b - b - V)(e^{\frac{qV}{kT}} - 1)}{Le^{\frac{qb}{kT}}(e^{\frac{q(\varphi_b - b)}{kT}} - e^{\frac{qV}{kT}})} \tag{6}$$

$$\phi_b = \phi_\infty - \phi_d - \phi_i - \phi_t$$

Where ϕ_∞ is the internal potential limit when $T \to \infty$ and can be considered as $\phi_\infty = \phi_{295} + \phi_{t,295} = \phi_{295} + \frac{1}{2}\frac{\sigma^2}{295k}$. If the distribution width of the density of states and the inter-site distance in the semiconductor are known, eq. 6 now gives a relation between the injection limited current and the barrier height. Importantly, eq. 6 shows the correct dependencies for injection currents in organic materials reported in literature, *e.g.* an injection efficiency that depends linearly on the charge carrier mobility[12] , an exponential increase in the injection current with increasing electric field[13] and a current density inversely proportional to the device thickness.[14,15]

7.3 Results

To directly evaluate the applicability of equation 6, we first apply it to a very well-known polymer system. Poly(3-hexylthiophene) is one of the most studied conjugated polymer materials. It is known that for sandwich type diodes of P3HT an Au top contact gives rise to a small injection barrier.[16,17] Therefore we fabricated P3HT diodes with PEDOT:PSS and Au contacts. PEDOT:PSS provides an ohmic contact to the HOMO of P3HT and is therefore ideally suited as ohmic contact in these devices. Figure 3 shows the structure of this type of sandwich diode and the *J-V* measurements of such a diode. Since the space-charge limited current from the ohmic PEDOT:PSS contact is very well described[18,19], we can extract the relevant device parameters from the space-charge limited current and use them in eq. 5 to describe the injection current from the non-ohmic top contact. If we reconsider figure 1, in this device configuration the built-in voltage for the diffusion current from the PEDOT:PSS contact can also be regarded as the injection barrier for the current from the Au contact. Figure 3 shows the space-charge limited regime for positive voltages, from which the internal potential of this device can be determined through eq. 1. Since the other parameters in eq. 6 have been independently determined for this conjugated polymer, this allows us to directly evaluate the injection-limited current for negative voltages. The solid lines in figure 3 show the fits using eq. 5 to the injection-limited current. Excellent agreement between the experimental and calculated current is found due to the barrier lowering terms of eq. 3-5. Table 1 gives an overview of all device simulation parameters used for this fit. This shows that eq. 6 properly describes the field and temperature dependence of the injection current.

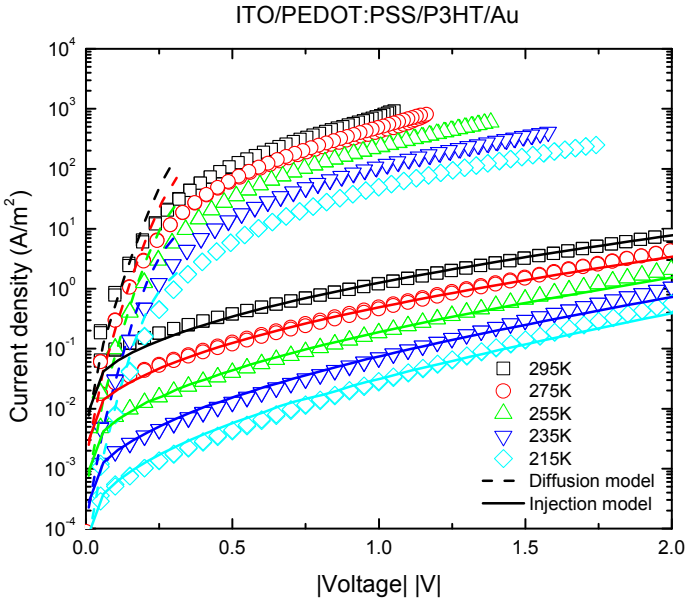

Figure 11. Temperature dependent current density-voltage characteristics of a single carrier P3HT device with PEDOT:PSS and Au contacts. The top symbols represent the space charge-limited current density from the ohmic PEDOT:PSS contact and the bottom symbols the injection limited current from the Au contact. The solid lines give the analytical fit to the injection current density.

Device thickness, d	110 nm
Dielectric constant, ε_r	3.0
Bandgap, E_{gap}	2.2 eV
Density of states, N	$3.0*10^{26}$ m^{-3}
Hole mobility, μ	$1.15*10^{-8}$ (295K) – $6.1*10^{-10}$ m^2 V^{-1} s^{-1} (215K)
Internal potential ϕ_{295}	0.2 eV

Table 1. Device simulation parameters.

Furthermore, to assess the dependence on barrier height of eq. 6, we fabricated P3HT diodes with TiO_x and MoO_3/Au contacts. TiO_x can be deposited using a sol-gel method by applying titanium isopropoxide on a substrate. It is known that TiO_x is a highly photosensitive compound whose work function can be

altered by exposure of the material to ultraviolet radiation. Molecular oxygen adsorbed to the surface of the TiO_x film can be removed by exposure to UV, thereby releasing an electron into the conduction band and raising the Fermi level. Using this phenomenon, a range of work functions can be created for the TiO_x contact. With MoO_3/Au as the ohmic hole contact, a geometry as in figure 1 can be created with a varying injection barrier for the non-ohmic contact in a single device. This enables direct evaluation of the injection barrier while all other device parameters remain constant. In particular the saturation current density can be deduced from eq. 1 by recognizing that for very small voltages we can apply a Taylor expansion around V = 0, which leads to:

$$J_p = \frac{q\mu_p N_v(\varphi_b - b - V)\left(\frac{qV}{kT}\right)}{Le^{\frac{qb}{kT}}\left(e^{\frac{q(\varphi_b - b)}{kT}} - \frac{qV}{kT} + 1\right)}. \tag{7}$$

Figure 4a shows the fit of eq. 7 to the current density in forward bias for the ITO/TiO_x/P3HT/MoO_3/Au device. In this way all device parameters are determined and the injected current density can be calculated with the help of eq. 3-6. Figure 4b shows the reverse bias current density with fits according to eq. 6.

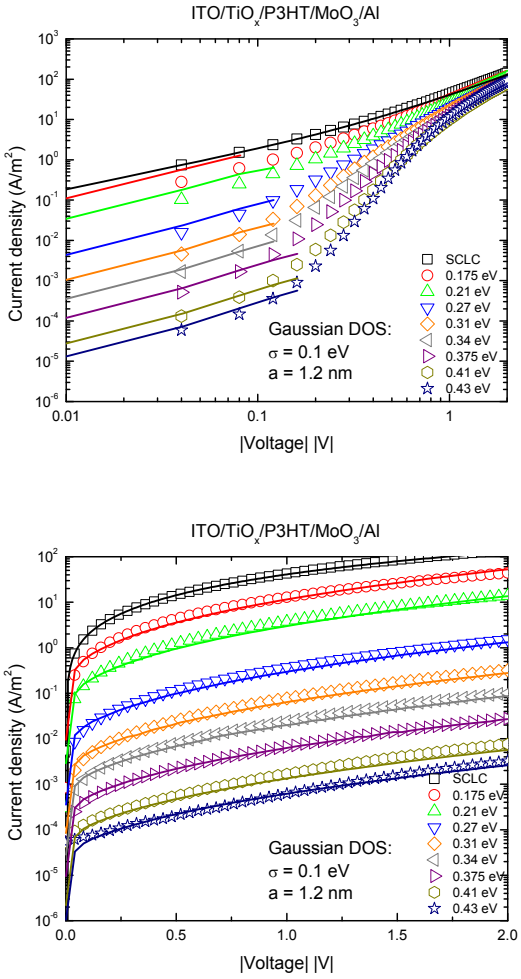

Figure 12. Forward current density characteristics and fits to the diffusion current of a TiO_x/P3HT/MoO_3 device according to eq.7 (a) and reverse bias injection current density with fits according to eq.6 (b).

7.4 Conclusions

We have demonstrated an analytical description for the injection currents in organic semiconductor diodes from a non-ohmic contact. Based on the description for diffusion currents with appropriate boundary conditions and accounting for the density of states in organic devices, the derivation is able to describe the temperature and field dependence of the injected current density across a potential barrier. Furthermore, the model is used to describe the injection currents in organic LEDs with a non-ohmic contact.

7.5 References

1. Schottky, W., *Naturwissenschaften* 26, (1938), 843–843.

2. Bethe, H. A. (Radiation Laboratory, Massachusetts Institute of Technology: 1942).

3. Rhoderick, E. H. & Williams, R. H. (Clarendon Press: 1988).

4. Crowell, C. R. & Sze, S. M., *Solid-State Electronics* 9, (1966), 1035–1048.

5. Arkhipov, V. I., Emelianova, E. V., Tak, Y. H. & Bässler, H. *Journal of Applied Physics* 84, (1998), 848–856.

6. Scott, J. C. & Malliaras, G. G., *Chemical Physics Letters* 299, (1999), 115–119.

7. Mihailetchi, V. D., Blom, P. W. M., Hummelen, J. C. & Rispens, M. T., *Journal of Applied Physics* 94, (2003), 6849–6854.

8. Simmons, J. G., *Journal of Physics and Chemistry of Solids* 32, (1971), 1987–1999.

9. Burin, A. L. & Ratner, M. A., *Journal of Polymer Science Part B: Polymer Physics* 41, (2003), 2601–2621.

10. Vissenberg, M. C. J. M. & Matters, M., *Phys. Rev. B* 57, (1998), 12964–12967.

11. Silver, M., Pautmeier, L. & Bässler, H., *Solid State Communications* 72, (1989), 177–180.

12. Shen, Y., Klein, M. W., Jacobs, D. B., Campbell Scott, J. & Malliaras, G. G., *Phys. Rev. Lett.* 86, (2001), 3867–3870.

13. Ng, T. N., Silveira, W. R. & Marohn, J. A., *Phys. Rev. Lett.* 98, (2007), 066101.

14. Rep, D. B. A., Morpurgo, A. F. & Klapwijk, T. M., *Organic Electronics* 4, (2003), 201–207.

15. Baldo, M. A. & Forrest, S. R., *Phys. Rev. B* 64, (2001), 085201.

16. Lyon, J. E., *et al. Applied Physics Letters* 88, (2006), 222109–222109–3.

17. Thakur, A. K., Mukherjee, A. K., Preethichandra, D. M. G., Takashima, W. & Kaneto, K., *Journal of Applied Physics* 101, (2007), 104508–104508–5.

18. Mihailetchi, V. D., Xie, H. X., de Boer, B., Koster, L. J. A. & Blom, P. W. M., *Advanced Functional Materials* 16, (2006), 699–708.

19. Goh, C., Kline, R. J., McGehee, M. D., Kadnikova, E. N. & Fréchet, J. M. J., *Applied Physics Letters* 86, (2005), 122110–122110–3.

Summary

Semiconducting metal oxide materials are becoming more and more prevalent in electronics, most notably in the area of displays, where transparent conductive materials are needed. But not only in the realm of inorganic semiconductors have metal oxides seen resurgence in the last decade. Since many metal oxides can be prepared through means of solution processing of precursor materials and subsequent hydrolysis and condensation, they are finding many applications in the field of organic electronics, where solution processing is the preferred choice of device fabrication. Of all transition metal oxides that find application, this thesis is focused on arguably one of the most studied materials of the past decade, zinc oxide (ZnO). This thesis describes a facile method of preparing ZnO thin films by applying a solution processed precursor film of zinc acetylacetonate hydrate, followed by mild annealing during which the precursor compound is hydrolyzed into ZnO.

Organic semiconductor devices that can be made with the ZnO films are described in chapter 2. First inverted organic solar cells with ZnO as electron extracting contact are demonstrated. It is shown that the performance of these devices rivals that of the conventional style devices, without the need for a low work function reactive metal contact.

Chapter 3 describes the material characterization of thin films fabricated by the aforementioned method. Characterization methods such as optical microscopy, ultraviolet-visible absorption spectroscopy (UV-vis), Fourier transform infrared spectroscopy (FTIR), X-ray diffraction (XRD), thermal gravimetry (TGA-DSC), atomic force microscopy (AFM) and scanning electron microscopy (SEM) combined with a focused ion beam (FIB) are applied to ascertain the material properties of the thin films. This exhaustive characterization reveals a decomposition of the precursor into ZnO, with a competition between hydrolysis and sublimation that is dependent on the atmospheric partial water pressure. Furthermore the fabricated ZnO thin films show very broad and weak X-ray diffraction peaks, indicating a largely amorphous or very fine grained material. Additionally the FTIR measurements suggest the presence of an impurity that can most likely be identified as hydrozincite, a hydroxycarbonate species of zinc. This compound can very easily be formed on ZnO surfaces in the presence of atmospheric CO_2 and

H_2O. The combination of AFM and FIB/SEM measurements shows a very smooth and flat thin film, with a surface roughness less than 2 nm.

To illustrate the advantages of this point further, organic light emitting diodes (OLEDs) are fabricated with ZnO electron injecting contacts, as shown in Chapter 4. The OLEDs with a polyfluorene copolymer PF10TBT show performance equaling that of OLEDs with a reactive metal electron injecting contact. Moreover the ambient stability of these OLEDs while under operation is shown to be greatly enhanced compared to their conventional counterparts. In Chapter 5 tandem solar cells are fabricated in an architecture that relies on the use of ZnO in the middle charge recombination electrode. The method to fabricate ZnO thin films described in this thesis can be employed to form thin films in this structure, replacing the traditionally used nanoparticles for this layer. The tandem devices show identical performance to tandems with nanoparticle layers. Furthermore the thin films can be used in a new inverted style tandem geometry that broadens the choice of materials in the organic bulk heterojunction solar cells making up the tandem device.

Chapter 6 deals with the internal potentials that are present in metal-insulator-metal devices; more particularly in organic devices with one Ohmic and one non-Ohmic contact. It is shown that in the context of the classical diffusion theory, assuming appropriate boundary conditions and accounting for band bending caused by charge carrier diffusion from an Ohmic contact into the organic semiconductor, the diffusion current can be accurately described. Furthermore it is shown that for organic devices with one non-Ohmic metal oxide contact the internal potential is dictated by the relative energetic positions of the organic material frontier orbitals and the Fermi level in the non-ohmic contact.

The charge injection properties of non-ohmic contacts into organic semiconductors are explored in chapter 7. It is shown that the theoretical framework developed in chapter 6 can be applied to account for injection-limited currents in organic semiconductor devices as well. A charge carrier diffusion-limited current model is developed, including special considerations for the broadly distributed density of states in the organic semiconductor. It is shown that the diffusion-limited injection current model, with inclusion of a field-dependent barrier lowering term that accounts for the probability of injecting through a low-energy pathway in the tail-states of the organic

semiconductor, can effectively account for the observed injection-limited currents in organic semiconductor devices. Furthermore, the implications of this model for OLEDs based on polymer materials that exhibit strong charge trapping is presented. It is demonstrated that the luminescent efficiencies of OLEDs with a non-ohmic contact do not decrease until the charge injection barrier is sufficiently high that the contact cannot supply the necessary amount of charge carriers to sustain the trap-limited bulk current. This implies that for OLED devices that inherently possess deep electron traps, a certain electron injection barrier can be tolerated before luminescent efficiency decreases. This finding has large implications for the choice of electron injecting contact material, since materials with larger work functions that are more stable to oxidation may be chosen, without losing device efficiency.

Samenvatting

Halfgeleidende metaal oxides worden alsmaar belangrijker in elektronica, vooral op het gebied van beeldschermen, waar transparante geleidende materialen benodigd zijn. Echter hebben metaal oxides niet alleen in de wereld van de anorganische halfgeleiders een wederopstanding meegemaakt. Omdat veel metaal oxides vervaardigd kunnen worden door een hydrolyse reactie van uit oplossing aangebrachte metaal complexen, vinden zij veel toepassingen in de organische elektronica, waar bij voorkeur materialen vanuit een oplossing aangebracht worden. Van alle halfgeleidende metaal oxides die een toepassing vinden, is dit proefschrift gericht op wellicht het meest onderzochte materiaal van het afgelopen decennium, zink oxide (ZnO). Dit proefschrift beschrijft een eenvoudige methode om dunne ZnO lagen te vervaardigen door een laag van acetylacetonaat hydraat uit oplossing aan te brengen en deze vervolgens door een milde verhitting te hydrolyseren naar ZnO.

Organische halfgeleider devices die met de dunne ZnO lagen gemaakt kunnen worden worden beschreven in hoofdstuk 2. Als eerste worden organische zonnecellen met ZnO als elektron extractie laag gedemonstreerd. De efficiëntie van deze zonnecellen is gelijk aan de efficiëntie van conventionele organische zonnecellen, terwijl het gebruik van een lage werk-functie reactieve metaal cathode hiervoor niet benodigd is.

Hoofdstuk 3 beschrijft de materiaal karakterisatie van dunne lagen die op de eerder genoemde manier zijn vervaardigd. Karakterisatie methoden zoals optische microscopie, absorptie spectroscopie (UV-vis), Fourier transform infrarood spectroscopie (FTIR), röntgen diffractie (XRD), thermische gravimetrie (TGA-DSC), atomische kracht microscopie (AFM) en electron microscopy (SEM), gecombineerd met een gefocuste ionen stroom (FIB) zijn toegepast om de materiaal eigenschappen van de dunne lagen te achterhalen. Deze uitputtende karakterisatie toont de decompositie van het voorloper materiaal naar ZnO, met een competitie tussen hydrolyse en sublimatie die afhankelijk is van de atmosferische waterdruk. De vervaardigde ZnO lagen vertonen brede en zwakke röntgen diffractie pieken, wat duidt op een grotendeels amorf materiaal of een zeer kleine korrelgrootte. Daarnaast suggereren de FTIR metingen de aanwezigheid van een onzuiverheid die geïdentificeerd kan worden als hydrozinkiet, een hydroxycarbonaat van zink.

Dit materiaal kan zich eenvoudig vormen op ZnO oppervlakken in de aanwezigheid van atmosferische CO_2 en H_2O. De combinatie van AFM en FIB/SEM metingen tonen een zeer vlakke en dunne laag, met een oppervlakte ruwheid van minder dan 2 nm.

Om de voordelen van deze aanpak verder de illustreren zijn organische licht-emitterende diodes met ZnO elektron injecterende contacten vervaardigd, beschreven in hoofdstuk 4. OLEDs met het polyfluorene copolymeer PF10TBT laten een efficiëntie zien die gelijk is aan OLEDs met een lage werk-functie reactieve metaal cathode. Daarenboven is de operationele stabiliteit van deze OLEDs sterk verbeterd ten opzichte van de conventionele OLEDs. Daarna worden in hoofdstuk 5 tandem zonnecellen getoond die vervaardigd kunnen worden in een geometrie die op het gebruik van ZnO in de midden elektrode berust. De methode om ZnO lagen te maken zoals deze in dit proefschrift is beschreven kan gebruikt worden in deze structuur, waarbij de traditioneel gebruikte nanodeeltjes voor dit doel vervangen kunnen worden. De tandem zonnecellen hebben een energie omzettings efficiëntie die gelijk is aan tandem zonnecellen met nanodeeltjes lagen. Bovendien kunnen de dunne lagen gebruikt worden in een nieuwe geïnverteerde stijl tandem geometrie die de materiaalkeuzes voor de organische bulk heterojunctie zonnecellen die onderdeel uitmaken van de tandemcel uitbreidt.

Hoofdstuk 6 gaat over de interne potentialen in metaal-isolator-metaal devices; in het specifiek in organische devices met één Ohms en één niet-Ohms contact. In de context van de klassieke theorie van ladingsdragers diffusie kan de diffusiestroom door de organische halfgeleider beschreven worden, mits de juiste randvoorwaarden gekozen worden en bandbuiging door gediffundeerde ladingen vanuit het Ohmse contact in ogenschouw wordt genomen. Hieruit blijkt dat voor organische devices met één niet-Ohms contact de interne potentiaal bepaald wordt door het energetische verschil tussen de moleculaire orbitalen van het organische materiaal en het Fermi niveau van het niet-Ohmse contact.

De ladingsdragers injectie eigenschappen van niet-Ohmse contacten in organische halfgeleiders worden onderzocht in hoofdstuk 5. Hier wordt aangetoond dat het theoretische raamwerk dat in hoofdstuk 4 ontwikkeld is, ook gebruikt kan worden om injectie-gelimiteerde stromen in organische halfgeleiders te beschrijven. Een model voor de injectiestroom is ontwikkeld,

gebaseerd op ladingsdrager diffusie, met speciale aandacht voor de brede verdeling van de toestandsdichtheid in de organische halfgeleider. Er wordt aangetoond dat het diffusie-gelimiteerde injectie-stroom model de geobserveerde injectiestromen in organische halfgeleiders kan beschrijven, mits een elektrisch veld afhankelijke barrière verlagingsterm wordt ingevoegd om de waarschijnlijkheid van het creëren van een laag energetisch injectiepad in de staart van de toestandsdichtheid in ogenschouw te nemen. Daarnaast worden de implicaties van dit model voor OLEDs gebaseerd op polymeer materialen die onderhevig zijn aan ladingsvallen besproken. Er wordt laten zien dat de luminescente efficiëntie van OLEDs met een niet-Ohms contact niet daalt totdat de injectie barrière groot genoeg is dat het contact de ladingen niet meer aan kan leveren om de ladingsval-gelimiteerde stroom te onderhouden. Dit impliceert dat voor OLEDs met diepe elektron vallen, een zekere elektron injectiebarrière veroorloofd mag worden voordat de luminescente efficiëntie daalt. Deze conclusie heeft grote implicaties voor de keuze van elektron injecterend contact materiaal, aangezien materialen met een grotere werk-functie gekozen zouden kunnen worden, die minder gevoelig voor oxidatie zijn, zonder verlies van luminescente efficiëntie.

List of publications

A facile route to inverted polymer solar cells using a precursor based zinc oxide electron transport layer.
P. de Bruyn, D. J. D. Moet & P. W. M. Blom. *Organic Electronics* **11**, 8, (2010), 1419-1422.

All-solution processed polymer light-emitting diodes with air stable metal-oxide electrodes.
P. de Bruyn, D. J. D. Moet & P. W. M. Blom. *Organic Electronics* **13**, 6, (2012), 1023-1030.

Diffusion-limited current in organic metal-insulator-metal diodes.
P. de Bruyn, A. H. P. Van Rest, G. A. H. Wetzelaer, D. M. de Leeuw & P. W. M. Blom. *Physical review letters* **111**, 18, (2013), 186801.

Characterization of precursor-based ZnO transport layers in inverted polymer solar cells.
N. Grossiord, P. de Bruyn, R. Andriessen & P. W. M. Blom. *Journal of Materials Chemistry C* **2**, 41, (2014), 8761-8767.

High work function transparent middle electrode for organic tandem solar cells.
D. J. D. Moet, P. de Bruyn & P. W. M. Blom. *Applied Physics Letters* **96**, 15, (2010), 153504.

Enhanced efficiency in double junction polymer: fullerene solar cells.
D. J. D. Moet, P. De Bruyn, J. D. Kotlarski & P. W. M. Blom. *Organic Electronics* **11**, 11, (2010), 1821-1827.

Hole-enhanced electron injection from ZnO in inverted polymer light-emitting diodes.
M. Lu, P. de Bruyn, H. T. Nicolai, G. J. A. H. Wetzelaer & P. W. M. Blom. *Organic Electronics* **13**, 9, (2012), 1693-1699.

Improving the compatibility of fullerene acceptors with fluorene-containing donor-polymers in organic photovoltaic devices.
J. C. Kuhlmann, P. de Bruyn, R. K. M. Bouwer, A. Meetsma, P. W. M. Blom & J. C. Hummelen. *Chemical Communications* **46**, 38, (2010), 7232-7234.

Origin of the efficiency enhancement in ferroelectric functionalized organic solar cells.
K. Asadi, P. de Bruyn, P. W. M. Blom & D. M. de Leeuw. *Applied Physics Letters* **98**, 18, (2011), 85.

Acknowledgements

To say the least, this acknowledgement feels overdue. At the time of writing I find myself realizing how fast the last five years, and indeed the four years before that, have slipped by. In my time in the MEPOS research group many people have come and gone, including my promotor Paul Blom. Albeit not always easy, this situation has been a good exercise in performing research with a large degree of independence.

Firstly I would like to thank you, Paul, for your guidance and for taking the effort to come to Groningen to discuss with the group so many times over the course of my four years.

I also would like to extend my gratitude to all former group members from whom I learnt a lot. Especially I want to thank Date Moet, who started as my supervisor and later became my colleague and friend. It was always a pleasure working with you and much of my work was building on what you had already done. You were always a good example for me on how to do research in a highly methodological way.

I remember the spring of 2008 when I had my first discussions with Bert de Boer, assistant professor in the group at the time, about doing a PhD here. I found myself in good agreement with his view on research. This seemed fortuitous since it became clear shortly after my decision to join the group that my official promotor and head of the group, Paul Blom, would be leaving for a new opportunity and challenge. At the time it became clear to me that on a day-to-day basis Bert would be my first line of support after that. His passing so suddenly at the beginning of 2009 came as a tremendous shock to everyone. I have found myself missing his expertise on many occasions throughout my PhD, as well as missing him personally. Therefore I want to thank him for who he was and for all that might have been, were he still with us today.

I wholeheartedly want to thank my parents, Henk and Meta, and my brother and sister-in-law, Marco and Anna here. Without your support for my decisions in life, I probably would not have been where I am, nor be the person I am today. For that I will always be truly grateful.

Of course I am also indebted to all of my friends who have always given me pause to relax and unwind on our regular meetings; I have always greatly appreciated our friendship. Even if some of us are now separated by quite some distance, our bonds remain strong.

I also want to thank all of my current colleagues at GasTerra for making the continuation of my career path so enjoyable and for all the valuable lessons you have already taught me. You have helped play an important part in my personal development over the last few years.

Finally and most importantly I want to thank the most important person in my life. Kriszti, your smile forever warms my heart. Language falls short to express what you mean to me and I can no longer imagine a life without you. Thank you for who you are. You bring out the best in me.